Journal of the Brazilian Society of Mechanical Sciences and Engineering (2022) 44:339
https://doi.org/10.1007/s40430-022-03666-w

TECHNICAL PAPER

Parametric analysis to explore the viability of cold spray additive manufacturing to print SS316L parts for biomedical application

Amritbir Singh[1] · Parminder Singh[2] · B. S. Pabla[3] · Harpreet Singh[2] · S. Shiva[1]

Received: 3 March 2022 / Accepted: 1 July 2022 / Published online: 14 July 2022

Abstract
In the current work, high-pressure cold spray additive manufacturing (CS) is used to print SS316L samples to explore its potential as an AM technology for bio-implant applications. For comparison purposes, laser powder bed fusion (LPBF) is also used to print the samples. Porosity, microhardness, microstructure and young's modulus analysis of the printed materials were done. Subsequently, the influence of heat treatment on the characteristics of printed samples was analyzed after being subjected to two distinct kinds of heat treating environments, viz. cooling in air and furnace. The study results validated that the samples manufactured by the CS technique were more porous and rougher than the LPBF technique. Grain structure confirmed the presence of cellular sub-grains, dendrites, and melt pool boundaries in an as-fabricated LPBF sample. In as-fabricated CS, the microstructure consists of deformed multi-crystalline grains. Improvement in microhardness after heat treatment was observed in the LPBF samples, whereas CS exhibited less value because of the reduced effect of cold working. The heat treatment of CS samples with furnace cooling resulted in microhardness and Young's modulus comparable to that desired for the body implants. Therefore, this study opens a pathway to explore CS as a viable technique for manufacturing bio-implants with tailor-made porosity, hardness and Young's modulus by optimizing process parameters.

Keywords Additive manufacturing · 3D printing · SS316L · Selective laser melting · Cold spray · Porosity · Microhardness · Microstructure

1 Introduction

Additive manufacturing (AM) is an advanced tool for layer-by-layer fabrication of complicated geometries using computer-aided design (CAD). It has gained worldwide attention in recent years, and the sector has grown significantly due to its benefits. Complex components, as required in biomedical applications, indeed be made using this technology, which has caught the attention of both academic and industrial researchers because of its potential to save time, money, and resources [1, 2]. Among the most significant AM processes, LPBF is used to fabricate various biomaterials, such as SS316L, Co–Cr alloys, titanium and its alloys [3]. Many biomedical researchers have focused on materials fabrication using LPBF because of its sophisticated process engineering relevance in medicine. Also, the process has certain limitations like long processing time, the need for post-processing to reduce the residual stress formation, etc. [4]. Moreover, in LPBF, the only materials compatible with the technique can be processed. However, the processing is not viable for metals like magnesium with bone-like characteristics and

Technical Editor: Lincoln Cardoso Brandao.

✉ Amritbir Singh
2021rme1032@iitjammu.ac.in

Parminder Singh
parminder.19mez0008@iitrpr.ac.in

B. S. Pabla
bsp@nitttrchd.ac.in

Harpreet Singh
harpreetsingh@iitrpr.ac.in

S. Shiva
shiva.sekar@iitjammu.ac.in

1 Department of Mechanical Engineering, Indian Institute of Technology Jammu, Jammu, India

2 Department of Mechanical Engineering, Indian Institute of Technology Ropar, Rupnagar, India

3 Department of Mechanical Engineering, National Institute of Technical Teachers Training and Research, Chandigarh, India

copper with antibacterial properties [5]. Even though the biomedical industry is well established due to LPBF technology, there is always room for development in terms of functional performance of biomaterial.

Biological 'inertness' is a common denominator among the biomaterials that decide its utilization inside a human body [6]. Several implant materials are adapted from commercial materials with greater purity levels to prevent the production of harmful by-products and limit corrosion. Researchers in the area of biomaterials describe implant fabrication as a difficult task in terms of achieving the properties equivalent to the bone. However, considering it has so many possible uses and can help us live better lives is what makes it so fascinating. Complexities arise when biomaterials are combined with biological surroundings in an effort to extend the life and restore function to tissues and organs [7]. There are different challenges of the biomaterial, which have been focused on by various people in the past. Some significant challenges are related to orthopedics biocompatibility and its osseointegration with the corresponding bone [8]. Therefore, several works in the literature on orthopedic implants are mainly focused on increasing their biocompatibility [9]. Apart from achieving the essential biocompatibility using the surface engineering approach, some inherent problems are noticeable in orthopedic applications, specifically the hardness mismatch and the stress shielding of the bone and implant [10, 11]. According to the research, the average hardness of bones varies by anatomical area and is between 33.3 and 43.8 HV [12]. Numerous investigations on other biomaterials show that hardness levels differ significantly in relation to bone hardness. For instance, Attar et al. [13] evaluated the hardness value of LPBF made titanium-based biomaterial part to be in the range of 235–266 HV. On the other hand, using the same process, SS316L hardness value is investigated by Cherry et al. [14], Li et al. [15], Kong et al. [16] and Liu et al. [17] reported the maximum value to be 225, 255, 280 and 216 Hv, respectively. Moreover, in work by Bedmar et al. [18], the microhardness of the SS316L produced using LPBF with a CO_2 and fiber laser is explored along with its comparison with the directed energy deposition (DED) technique. The DED sample has the lowest hardness at 221 HV, while the fiber laser-based LPBF sample has the highest, at 289 HV. According to the stated figures, bone hardness is much lower than the reported values. Consequently, the claimed biomaterial hardness measurements are troublesome in terms of their capacity to penetrate deeply into the bone.

Moreover, the stress shielding between implant and bone is a detrimental consequence besides hardness mismatch. Stress shielding is the loss of bone density caused by an implant removing the usual stress of the bone [19]. This is due to Wolff's law, which states that bone in a healthy human or animal will rebuild in response to the pressures imposed on it [20]. Implants that are too rigid affect the distribution of stresses in the connected bone. Owing to the significant variation in the stress distribution (high stress on implant and low on interconnected bone), bone resorption occurs. Therefore, to overcome such problems, it becomes evident to reduce the difference between elastic modulus values of implant and bone that are in contact with each other. In one of the studies, the LPBF technique is utilized to form SS316L samples by Rottger [21], in which four different samples are formed at optimized parameters, each made using different machines. Each sample's elastic modulus is computed in vertical and horizontal directions. The results obtained in this study are between the range of 141.2 and 205 GPa, which is considerably distinct from the bone modulus. Similarly, the same approach of using different machines of LPBF is opted to evaluate the mechanical properties of SS316L in the recent study reported by Obeidi et al. [22]. This study distinguishes from Rottger [21] by providing details on the effect of parameter variation of each machine on the mechanical properties. According to the findings, depending on the machine and process parameter used, the elastic modulus changes from 54 to 214 GPa. The Concept Laser M1 and ProX 200 machines achieve the lowest and highest modulus values. It is observed that the minimum value of modulus relates to the low density of the part. Therefore, introducing the intentional pores to the implants will aid in modulus reduction [23, 24]. In lee et al. [25] work, porous and biomimetic titanium scaffolds with drastically variable pore properties have been successfully manufactured. These components' mechanical characteristics are suitable for use as bone replacements. Owing to the highly porous nature of the scaffolds, the stiffness values are reported in the range of 11.7 to 17.4 GPa, which is equivalent to the cortical bone stiffness.

Surface quality is one implant-related feature that is thought to be critical for optimal implant integration in live bone. The rough surface of the implant increases osteogenic differentiation and enhances the surface area, increasing the likelihood of biomolecule loading and cell interaction sites [25]. The literature reported different studies on this aspect of surface roughness and its usefulness in biomedical applications. Tuan and Grofiner-Schreiber [26] investigated osteoblasts grown on smooth, uneven, and porous titanium samples. The findings demonstrated that cells cultured on rough surfaces had much greater collagen production and mineralization capabilities rates than cells on smooth samples. However, it is pertinent to state that in the mentioned study, scanning electron microscope (SEM) is the sole technology employed to characterize surface topography. Further, in the study by Haslauer et al. [27], the sample of Ti6Al4V is prepared using a direct metal fabrication technique, and they assessed its biocompatibility in a porous and solid unpolished state. With the mean roughness (Ra) value of 34–40 μm, the human adipose-derived adult stem cells (hASCs) had survived and grown on the samples even after 8 days exhibiting significantly superior biocompatibility than the conventionally made polished sample. A study by Martinet et al. [28] compared the proliferation and differentiation of cells in contact with titanium surfaces with varying surface roughness. It is revealed that the differentiation of cells and dissolution of the matrix are affected by the regularity and surface roughness. On the other hand, cells grown on rough surfaces (18.28 μm) were shown to produce more matrix and collagen.

The previously published hardness and elastic modulus values suggest the unavoidable property variation. This variance increases the likelihood of the implant penetrating the bone, resulting in unwanted and perhaps dangerous complications along with stress shielding. Moreover, the requirement of surface roughness and porosity are considered righteous in the biomedical application. Consequently, understanding the level of property mismatch and requirement of some indispensable attribute like surface roughness and porosity, necessitates the use of additional types of processing technologies in implant manufacture.

Cold spray (CS) technology began in the late 1980s [29]. Supersonic velocity is achieved through propulsion of a process gas (usually nitrogen or helium) by use of a De-Laval jet nozzle. This supersonic jet of gas subsequently accelerates the feedstock of micro-sized metallic powder to a high velocity. These high-velocity powder particles subsequently impact the substrate and deposit on it at temperatures below the melting point of the feedstock material. The aggregation of CS deposits is determined by particle kinetic energy and the subsequent permanent deformation of the particle striking the substrate [30]. CS provides other unique advantages over fusion-based methods, such as decreased thermal disruption impacts, no oxidation effect, no phase transition and the opportunity to repair damaged components [31]. With technological advancement, cold spray (CS) has evolved in the past few years. Due to the CS process increased mobility by a 6-axis robot, its usage in freeform manufacturing is currently acknowledged [32]. Given its capacity to deposit thick layers of various materials, some researchers have recently investigated the potential of CS for printing 3D freestanding parts. Apart from thick layer consolidation, it is widely used in complicated part creation by companies such as Spee3d [33], Titomic [34], and others [29]. The need for the mentioned evolution can be attributed to the advantages offered by CS, for instance, high deposition rates, less production time, flexibility in processing several metals and their alloys etc.

The literature reviewed above indicates that a high hardness and elastic modulus value in LPBF will offer the mismatch of mechanical properties between the bio-implant and bones, resulting in stress shielding. On the other hand, CS, an emerging technology, has applications extended to additive manufacturing. Hence, the present study is planned to evaluate the compatibility of the CS technique as 3D printing technology to fabricate standalone SS316L samples compared to LPBF in terms of porosity, microhardness, elastic modulus and microstructure to explore the use of CS for developing bio-implants.

2 Methodology

2.1 Feedstock powder

Spherical-shaped SS316L (PLM-316AA) powder was used as the feedstock material to print samples by LPBF and CS techniques. The powder was supplied by LPW Technology Limited, UK. The EDS (energy-dispersive spectroscopy) integrated with scanning electron microscope (SEM) [JEOL, JSM-6610LV, Japan] was used for composition analysis of the powder, as shown in Table 1 and Fig. 1. The powder had a purity of 99.9%, with an average particle size of 23.5 μm.

The morphology of the feedstock was confirmed to be spherical by SEM (JEOL, JSM-6610LV, Japan), Fig. 2a. The particle size distribution (Fig. 2b) was evaluated with ImageJ software, which shows that 86% of the powder particles have an average diameter in the range of 11–40 μm. Moreover, the presence of satellite and dendrites was observed in the magnified image. Therefore, owing to their occurrence, particles seem rough. This roughness has implications for powder flowability, but as far as biomedical applications are concerned, it helps increase biocompatibility [25, 35]. Hence, employing such feedstock in the processing technologies is an added advantage in this study.

2.2 Development of SS316L samples

Fabrication of SS316L samples, each having measurements of $20 \times 60 \times 5$ mm^3, was done utilizing an LPBF system (EOS GmbH, EOSINT M 280, Germany), having a working

Table 1 Composition of SS316L feedstock material used to fabricate samples by laser powder bed fusion (LPBF) and cold spray (CS) processes

Elements	Fe	Cr	Ni	Mo	Mn	Si	C	P	S
% age (by weight)	68.22	17.05	10.30	2.39	1.56	0.40	0.03	0.03	0.015

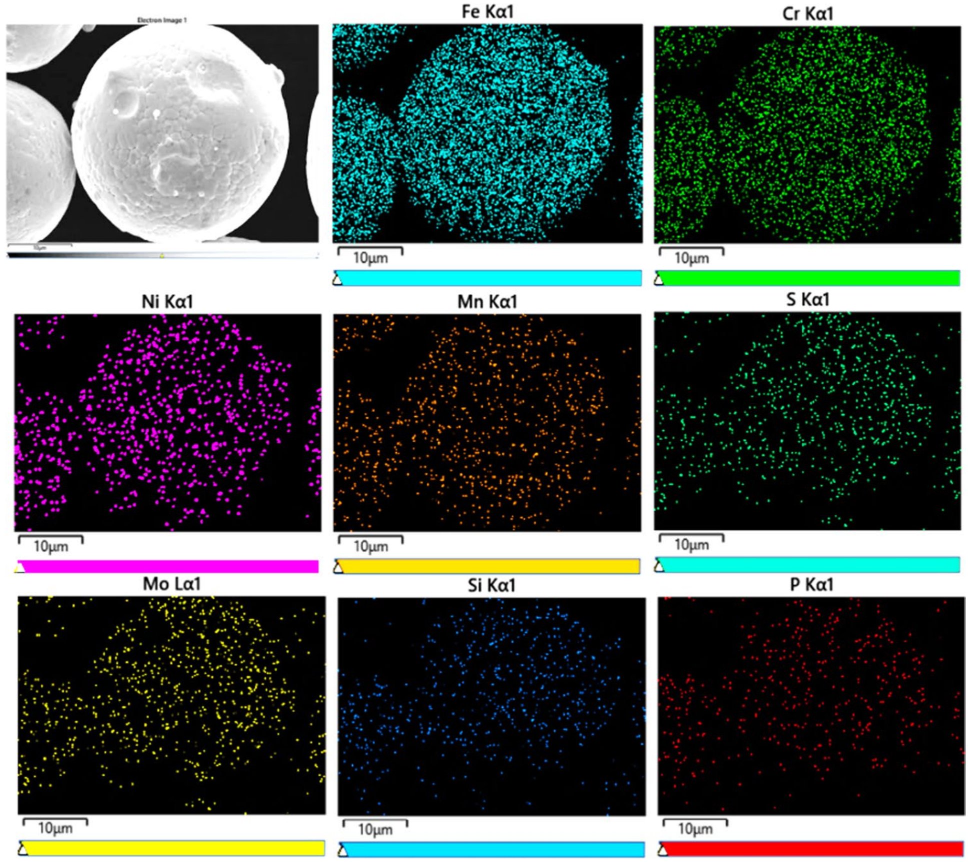

Fig. 1 The color-coded image of different compositions of SS316L powder used to print samples by laser powder bed fusion (LPBF) and cold spray (CS) techniques

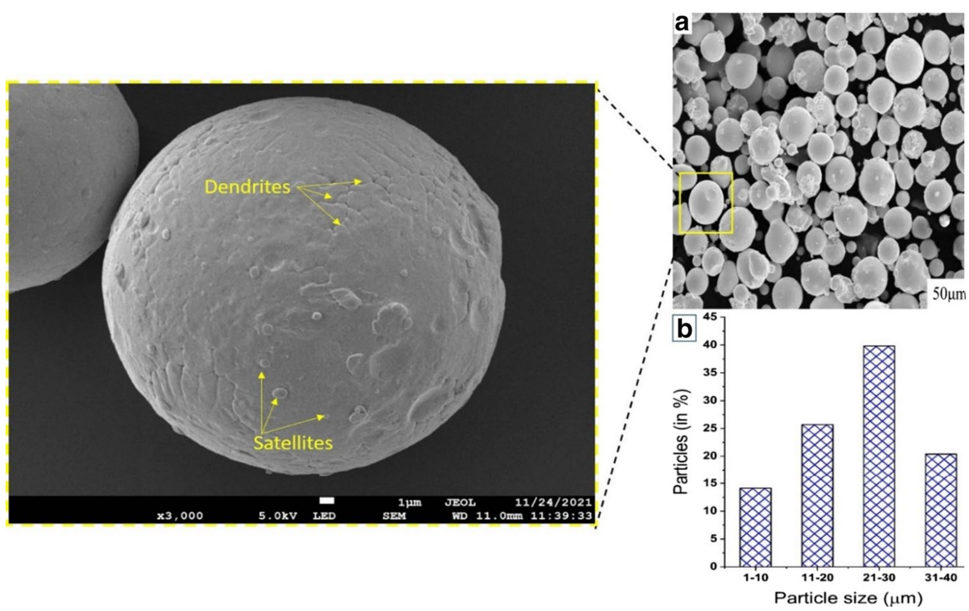

Fig. 2 **a** Surface morphology with single-particle magnified image and **b** particle size distribution of SS316L powder used to print SS316L samples by laser powder bed fusion (LPBF) and cold spray (CS) techniques

volume of 250 × 250 × 325 mm^3. An argon environment with less than 1% oxygen content was used during manufacturing, whereas the substrate was medium carbon steel of grade C45. The printing was done at the process parameters (Table 2) on the EOS M280 machine, using a Yb-fiber laser (wavelength 1060–1100 nm). The process variables were then compared with the normalized model-based processing graph by Thomas et al. [36]. This graph defines the feasible processing window for various materials, including SS316L. The chart was created between the dimensionless quantities

Table 2 Process parameters used to print SS316L samples with the aid of laser powder bed fusion (LPBF) technique

Spot diameter	Laser power	Layer thickness	Hatch spacing	Scanning speed	Inert gas used	Scanning Strategy
0.1 mm	210 W	0.04 mm	0.09 mm	900 mm/s	Argon	Zig-Zag

of E(min) (x-axis) and 1/h* (y-axis). The E_{min} represents the minimal heat necessary to bring the powder bed temperature to the material's melting point within a particular laser scan line so as to prevent void formation [26]. Hence, E(min)is given by

$$E(\min) = \left[A \times \frac{\mathrm{q}}{2 \times \mathrm{v} \times \mathrm{l} \times \mathrm{r}}\right]\left[\frac{1}{\rho c(\mathrm{T1} - \mathrm{T0})}\right]$$

where A is surface absorptivity (0.53 for LPBF), q is the laser/electron beam power (W), v is scanning velocity (m/s), l is layer height (m), r is spot radius (m), ρ is the density of solid SS316L feedstock (kg/m^3), c is specific heat (J/kg.K), T1 is the melting temperature of SS316L (K), and T0 is the bed temperature (K).

On the other hand, 1/h*indicates the size of the hatch spacing compared to the laser spot radius, with the bulk of tests carried out in the 0.6–1.5 range. It is given by

$$\frac{1}{\mathrm{h}^*} = \frac{r}{h}$$

where h is the hatch spacing (m).

In the current investigation, E(min) and 1/h* values were 5. 62 and 0.55, respectively. Plotting the same values in the normalized graph showed the parameter selected in the present study was out of the feasible processing window for the SS316L material and lies in the porosity regime. Although the mentioned parameters were not acceptable for load-bearing applications, however, as far as biomedical applications were concerned, porosity was the essential trait, and therefore the selected variables were considered righteous for LPBF part printing.

Another set of SS316L specimen samples with dimensions of 25 × 30 × 1 mm^3 was printed with the help of a high-pressure cold spray technique (Plasma Giken, PCS-100, Japan) available at IIT Ropar (India). In this system, a tungsten-made convergent-divergent nozzle (Plasma Giken, PNFC2-010-20S, Japan) was expended to speed up the powder feedstock with the help of nitrogen as a carrier gas. Table 3 provides the process parameters employed to print the samples. The samples printed by LPBF and CS are designated as as-fabricated (AF) in this work.

2.3 Surface roughness

Prior to the required heat treatment of the samples fabricated using the CS and LPBF technique, the surface roughness of the as-fabricated samples was measured using an optical microscope (OLYMPUS, TSX 5100, Japan). The device assessed surface roughness in terms of the average value (R_a) in micrometers in a quick and accurate manner. The aerial roughness of the samples reported in the study was taken from the area of dimensions 1994 × 1994 µm^2. However, to obtain the precise measurements, the roughness values represented were the average of 10 readings taken at different locations. Moreover, the surface topography images were obtained from the same device and scanning electron microscope [JEOL, JSM-6610LV, Japan].

2.4 Heat-treatment

Following the 3D printing, the as-fabricated LPBF and CS samples were cut into smaller samples each of size 20 × 20 mm × 5 and 25 mm × 10 × 1 mm, respectively, with a Wire EDM [Makino, UP6 H.E.A.T., Japan]. Photographs of the samples are shown in Fig. 3. Subsequently, heat treatment on these samples was performed at a temperature of 1100 °C using a Muffle furnace (ENKAY, 155P, India). This temperature was chosen in the light of an earlier study by Salman et al.[37], according to which a microstructure with relatively higher porosity could be achieved above 1000 °C. After heating in the furnace, one set of samples each from LPBF and CS was air-cooled, while the other one furnace cooled. The soaking time for low carbon steel was decided based on the thickness of the specimen, as advised in the ASM handbook [38]. The usual thumb rule is 1 h/inch

Table 3 Process parameters used to print SS316L samples by cold spray (CS) technique

Nozzle	Carrier gas	Gas pressure	Gas temperature	Stand-off distance	Gun transverse speed	Number of passes	Step size	Powder feed rate
Tungsten Convergent-Divergent	Nitrogen	50 bar	873 K	25 mm	0.3 m/s	15	1.5 mm	20 g/min

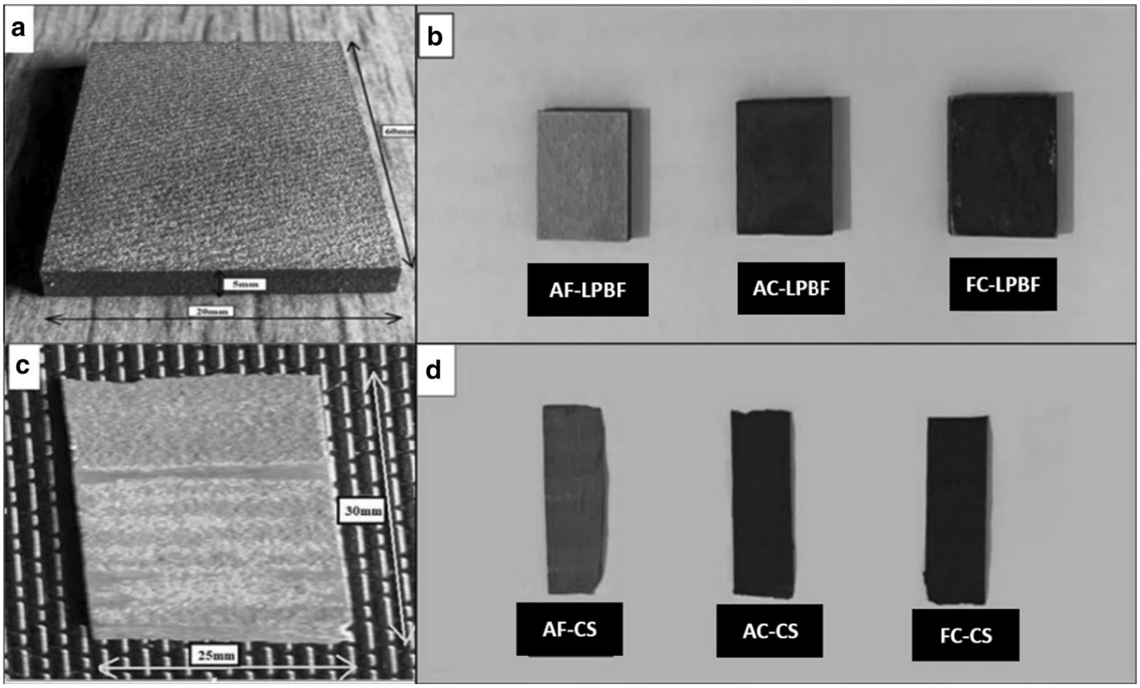

Fig. 3 Photographs of SS316L as-fabricated and heat-treated samples printed via (**a**,**b**) laser powder bed fusion (LPBF) and (**c**,**d**) cold spraying (CS) techniques before (**a**,**c**) and after (**b**,**d**) wire-cut EDM cutting and heat treatment

thickness of the specimen and thus obtained soaking time as given in Table 4. The table also shows a designation system for the various specimen materials used in the present study. Moreover, to decrease implant-level wear and corrosion, surface-modification methods may be applied. Eventually, increasing the thickness of the surface oxide layer may help enhance the resistance to corrosion of metallic materials and their biocompatibility [39, 40]. Therefore, in the present study, the thermal treatment in the oxygen-rich environment is carried out, followed by the furnace and air cooling to develop the required thick oxide layer.

2.5 Materials characterization

A scanning electron microscope [JEOL, JSM-6610LV, Japan] and an optical microscope [LEICA, DM2700 M, Germany] were used to analyze the microstructures and porosity of the LPBF and CS samples. The CS samples were mounted and polished as per the standard metallurgical procedure. To expose the grain structure, the samples were chemically etched using 45 ml HCl, 15 ml HNO3 and 20 ml methanol. A free and open-source image analysis tool (ImageJ) evaluated the apparent surface porosity in the CS and LPBF samples by converting their micrographs into binary format. The porosity values reported for each sample are an average of the five randomly selected images taken by the optical microscope. Apart from this, the X-ray diffraction (XRD) machine (MALVERN PANALYTICAL, EMPYREAN, UK) was also used to examine the various phases formed. The readings in XRD were determined using the Bragg–Brentano scanning method with a scanning angle of 20°-90° and step size and time of 0.01° and 20 s, respectively.

Table 4 Designation systems and heat-treatment parameters used for various SS316L specimen materials used in the current study

Description of the printed samples	Designation	Heat-treatment temperature	Soaking time
LPBF	AF- LPBF	N/A	N/A
Air-cooled LPBF	AC- LPBF	1100^0C	12 min for 5 mm thickness
Furnace-cooled LPBF	FC- LPBF	1100^0C	12 min for 5 mm thickness
CS	AF- CS	N/A	N/A
Air-cooled CS	AC- CS	1100^0C	3 min for 1 mm thickness
Furnace-cooled CS	FC- CS	1100^0C	3 min for 1 mm thickness

2.6 Mechanical properties measurement

The hardness of the as-fabricated and heat-treated samples was determined using a Vickers microhardness testing equipment (MITUTOYO, Japan). A diamond indenter was used to exert a load of 0.5 kgf for a dwell duration of 10 s. Nine values were taken along the specimen length at the difference of 2 mm for each sample, and the average of these values is reported as the final microhardness value. Further, modulus of elasticity measurement was accomplished using a Nano indentation machine (HYSITRON, TI PREMIER, USA) at the indent load of 2 mN for almost 18 s. The final value of elastic modulus is the average of 5 indents taken randomly at different positions.

3 Results and discussion

3.1 Surface analysis of AF-CS and AF-LPBF

The indispensable information with respect to the surface is presented for AF-LPBF and AF-CS is shown in Fig. 4. In Fig. 4a, for AF- LPBF, the evident existence of surface beads is analyzed, which further provides the additional details of melt-pool width (0.133 mm) and scanning direction. Moreover, spherical balls are noticed at low magnification, providing a vague idea of their actual presence and shape. Although to make it more discernable, a high-magnification picture was used to confirm its (yellow arrow) occurrence (Fig. 4b). The existence of spherical balls can be ascribed to two reasons: the un-melted powder attached from the surrounding loose feedstock and the other due to well-established defects in LPBF known as balling phenomena [41]. In order to confirm the reason for its occurrence, the size of the balls was determined. The analysis shows the balls' size was within the particle diameter range, and therefore, its presence on the surface can be attributed to the sintering of loose feedstock.

In Fig. 4c), the surface image details of AF-CS are explored and analyzed. The low-magnification picture of the CS sample provides the vision of a large number of powder particles in a specified area. Howbeit, the magnified view (Fig. 4d) represents the necessary information concerning the severe plastic deformation of the SS316L

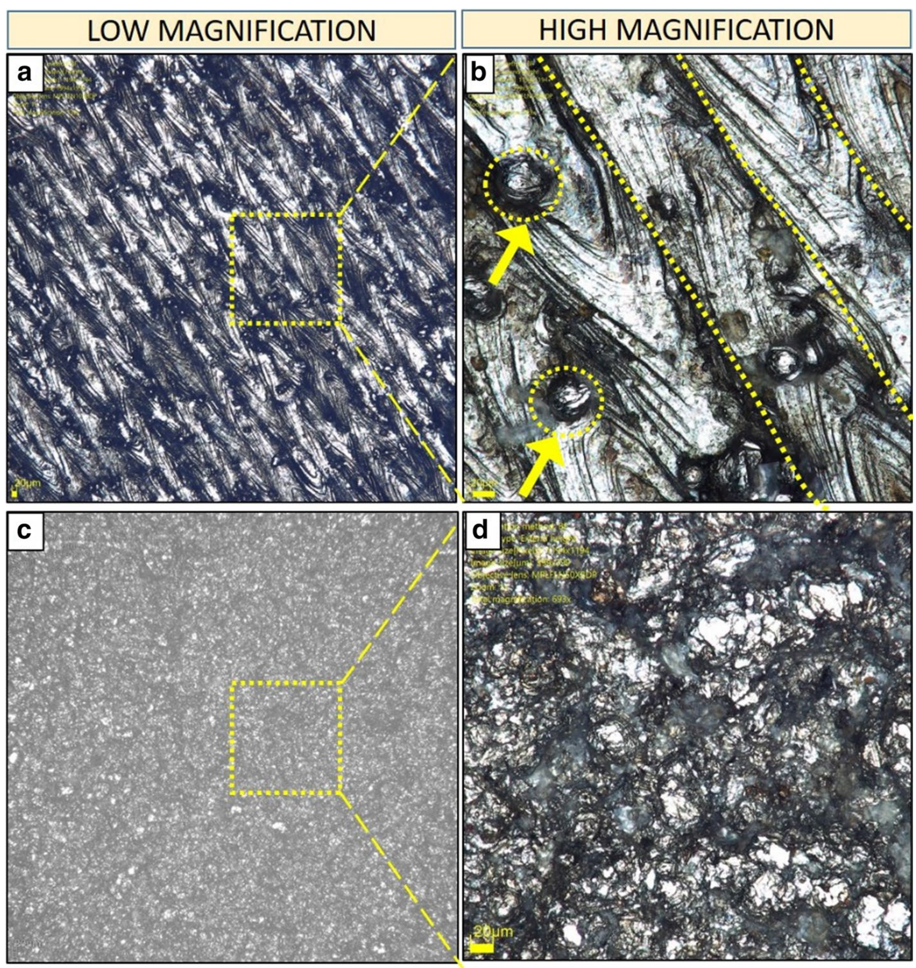

Fig. 4 Surface images taken using an optical microscope prior to heat-treatment and finishing operations of SS316L samples printed by (**a**,**b**) laser powder bed fusion (LPBF) and (**c**,**d**) cold spray (CS) in the as-fabricated (AF) state

particle at a high strain rate. The particle deposition is ascribed to the phenomena of adiabatic shear instability as reported in numerous past researches [42, 43]. Moreover, the extent of plastic deformation is significantly affected by the powder particle size; therefore, the non-uniformity in plastic deformation is evident because of the range of the particle sizes used in this study [44].

The aerial roughness of AF- LPBF is 44% lower than that in AF-CS. The low value in the former is ascribed to the complete melting of the feedstock material during processing. Besides, there still exists roughness of 6.38 μm in LPBF due to the presence of un-melted feedstock that can be observed in Fig. 5a,b. In the case of AF-CS, however, the essence of the process requires the use of high-velocity particles that attach when pounded over the substrate or already deposited particle. According to the bonding mechanism, the feedstock undergoes significant plastic deformation at the contact and produces a jet owing to strong shear stresses. This solid-state adhesion and jetting formation increase the roughness of the specimen [45]. Apart from this, the second possibility is related to the concept of coverage of feedstock particles over the area of deposition. The non-uniform coverage brings about the majority of feedstock deposition at certain areas, while others remain short of particle consolidation. Owing to this, the voids are created in the deposits, as shown in Fig. 5c,d.

Despite the fact that roughness is often believed to be the most critical factor in determining biocompatibility, there are certain publications in the literature that reflect the problems associated with the same. One crucial negative effect is the poor corrosion resistance associated with rough surfaces. Consequently, inflammation and unfavorable cellular responses may result from the deliverance of SS316L ions in the tissues owing to the localized corrosion of biomedical implants [46].

3.2 XRD characterization

Figure 6a shows the XRD analysis of the SS316L samples produced by LPBF and CS. For all CS samples and SS316L powder, the XRD pattern exhibits α and γ phases, with the γ component comprising a more significant volume percentage. Interestingly, in AF-CS, deformation-caused-martensitic phase transformations did not occur in spite of the elevated strain rates of the high velocity particles. Typically, when SS316L material is exposed to substantial levels of work hardening, it results in the phase transformation from austenite to martensite [47, 48]. This lack of phase change, however, may well be understood

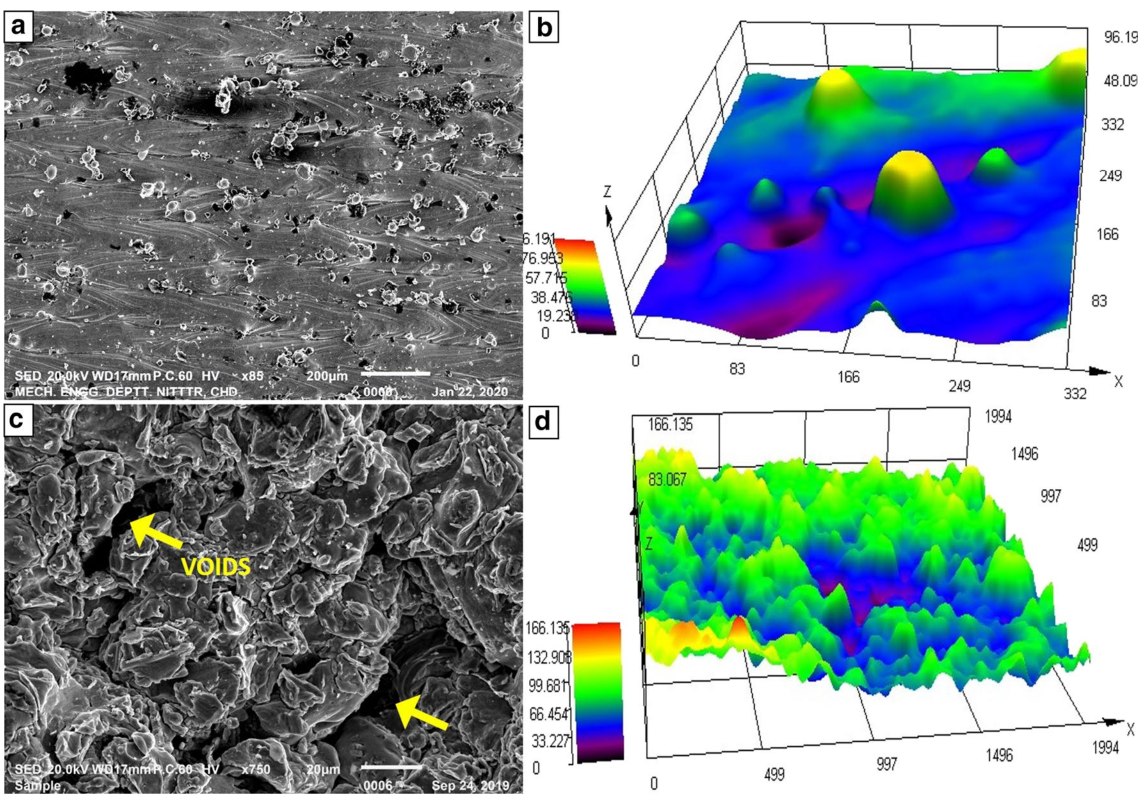

Fig. 5 Scanning electron microscope (**a**,**c**) and optical microscope color-coded topography images (**b**,**d**) of the samples in the as-fabricated (AF) form developed with the aid of (**a**,**b**) laser powder bed fusion (LPBF) and (**c**,**d**) cold spray (CS) technique

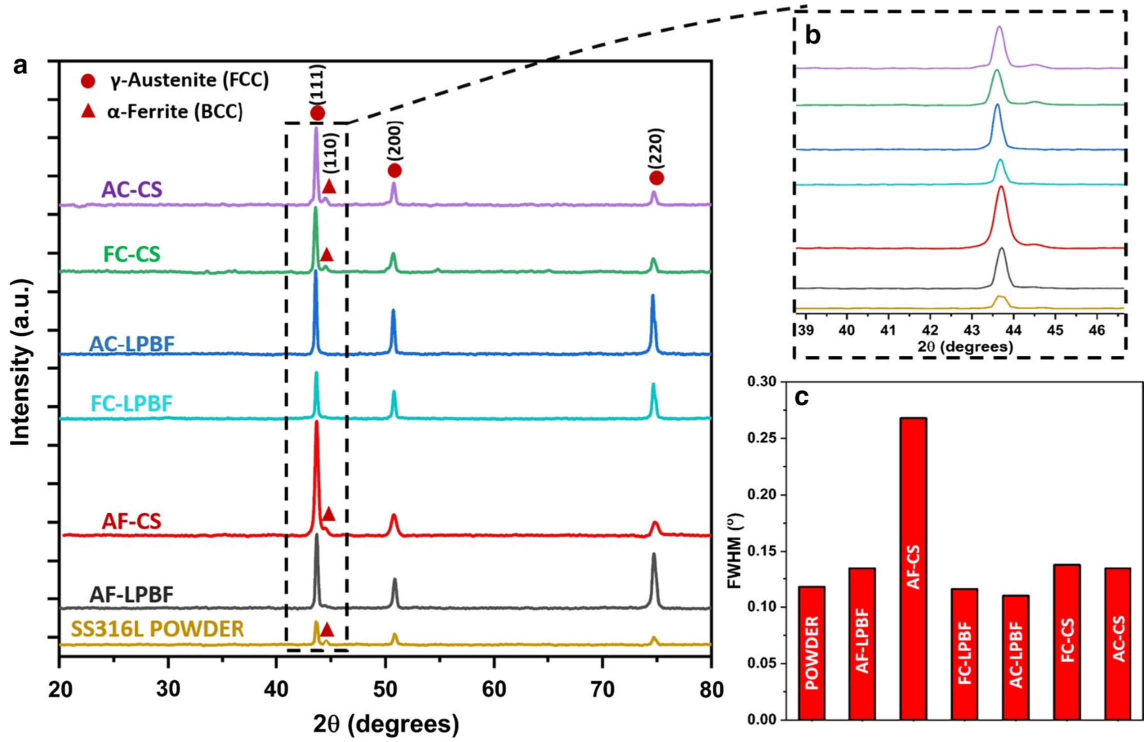

Fig. 6 The **a** XRD spectra of all the samples manufactured using laser powder bed fusion (LPBF) and cold spray (CS) technique with their respective designation along with the **b** enlarged view and **c** FWHM values at 43.58° angle

by the strain rates induced by CS. Generally, a martensite transition requires strain rates of 10^1 to 10^3 s^{-1} to be present during powder processing, while strain rates in CS are typically between 10^6 and 10^9 s^{-1}. As per the research conducted by Chen et al. [49], strain rates over the martensite formation range generate an abundance of dislocation twins that hinders the migration of surrounding dislocations, thereby negating its transition. The AF-LPBF sample, on the other hand, showed just one kind of phase, namely γ phase. Furthermore, in contrast to AF-LPBF, no discernible difference was observed in post-heat-treated LPBF samples (AC and FC-LPBF). The enlarged picture in Fig. 6b shows no noticeable peak shift in high-intensity peaks at a 43.58° angle. Furthermore, the FWHM values in Fig. 6c demonstrate that the AF-CS sample has considerable peak broadening. According to a Williamson–Hall plot analysis, the peak's expansion may be attributed to a combination of grain refinement and lattice microstrain, both of which are most likely caused by strain hardening in AF-CS. Slight and considerable reduction in the FWHM of AF-LPBF and AF-CS is observed in the post-processed samples, respectively. This reduction can be explained in terms of stress relieved during heat treatment resulting in lower FWHM values.

3.3 Porosity

Figure 7 illustrates the optical images of the CS and LPBF samples in their as-fabricated, air-cooled, and furnace-cooled conditions. The arrows in this figure indicate the porosity present in each specimen. The porosity of the AF-CS material is determined to be 6% (pore diameter of 32 µm), as seen in Fig. 7b, which is twice that of the AF-LPBF material (3% with an average diameter of 5 µm, as shown in Fig. 7a). The higher value in the former case could be attributed to the occurrence of cold-working during the CS process. During CS, the deposited particles possess plastically deformed morphologies due to high strain deformation without melting feedstock powder particles. Besides, by dint of improper plastic deformation of SS316L particles, the presence of pores was evident [50]. During cold spraying, this leads to the creation of a somewhat porous structure. It is relevant to mention that the porosity can be tailored to even higher values by optimizing the process parameters and average particle size distribution. In the context of bio-implants, it is pertinent to mention that higher porosity results in a greater surface area of the adsorbent, further aiding in the process of adsorption of cells. In contrast to the AF-CS, AF- LPBF (Fig. 7a) is less porous because the process leads to the

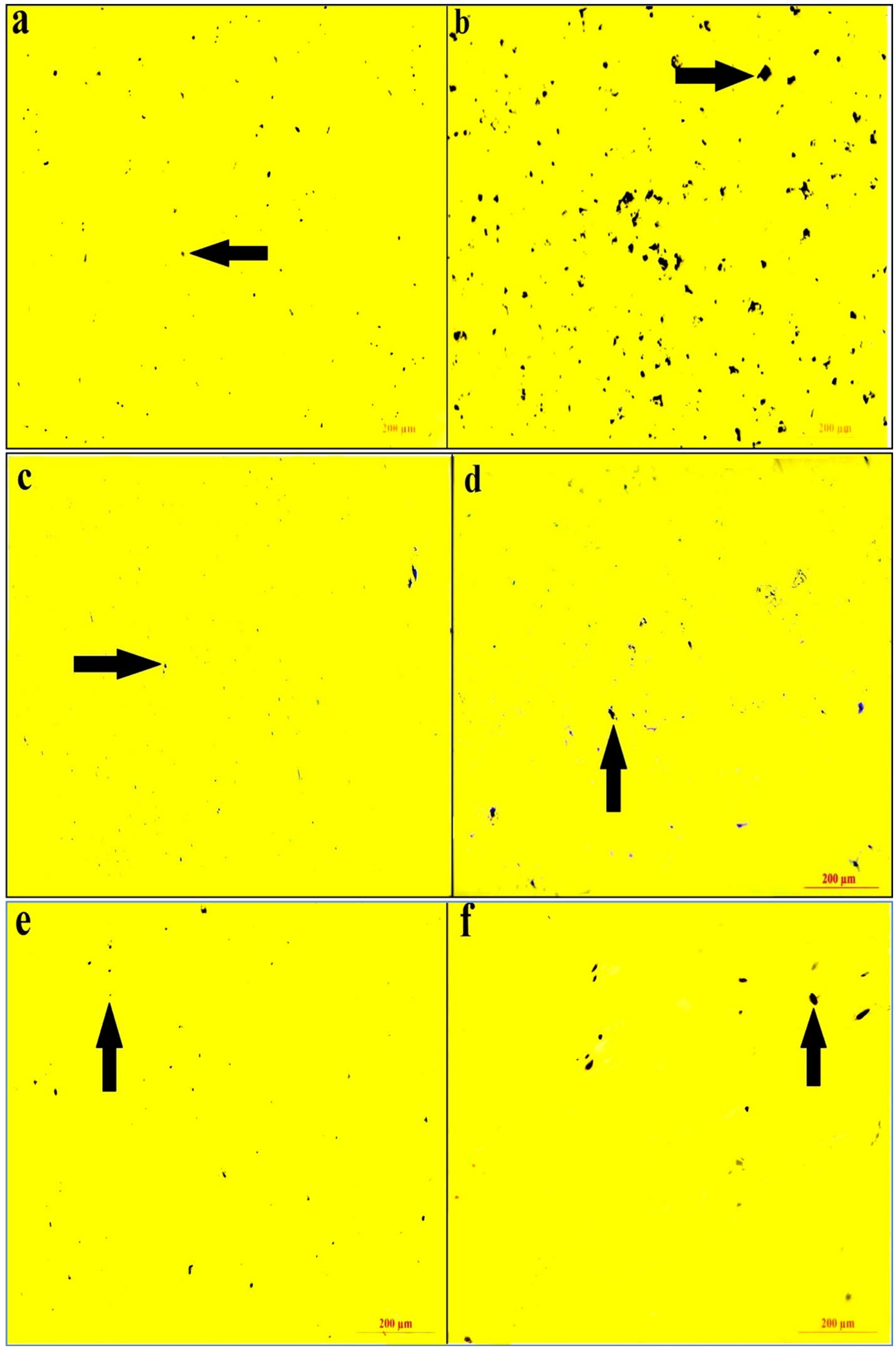

Fig. 7 Optical images of SS316L samples printed by laser powder bed fusion (LPBF) and cold spray (CS) in the as-fabricated (AF) state (**a**,**b**), thermal treatment followed by furnace-cooling FC- LPBF **c** and FC-CS **d** and thermal treatment followed by air-cooling AC- LPBF **e** and AC-CS **f**. Arrows indicate the pores formed

melting of the powder particles, resulting in the filling up of voids more easily and hence forming a relatively denser part. As far as porosity in LPBF is concerned, pore formation generally depends upon the melt track sections involving the laser's hottest spot depression, area of transition and region of tail [51]. The area under the immediate effect of laser undergoes indentation of powder layer that collapses due to change in the velocity vector field of laser [52–54]. This results in the entrapment of the gas bubbles forming pores inside the material. Sometimes, high temperature created due to laser power leads to vaporization of the material resulting in a vapor cavity [55].

Further, it is evident from Fig. 8a that heat treatment significantly drops porosity in all the investigated cases. It is well established that post-treatment reduces porosity due to inter-atomic diffusion at the grain (LPBF) or particle (CS) boundaries filling up pores present in the microstructures. Moreover, when the cooling starts, the outer layers of the samples cool first ensuing contraction in the inner hotter layers, thereby reducing the porosity. In the case of heat-treated

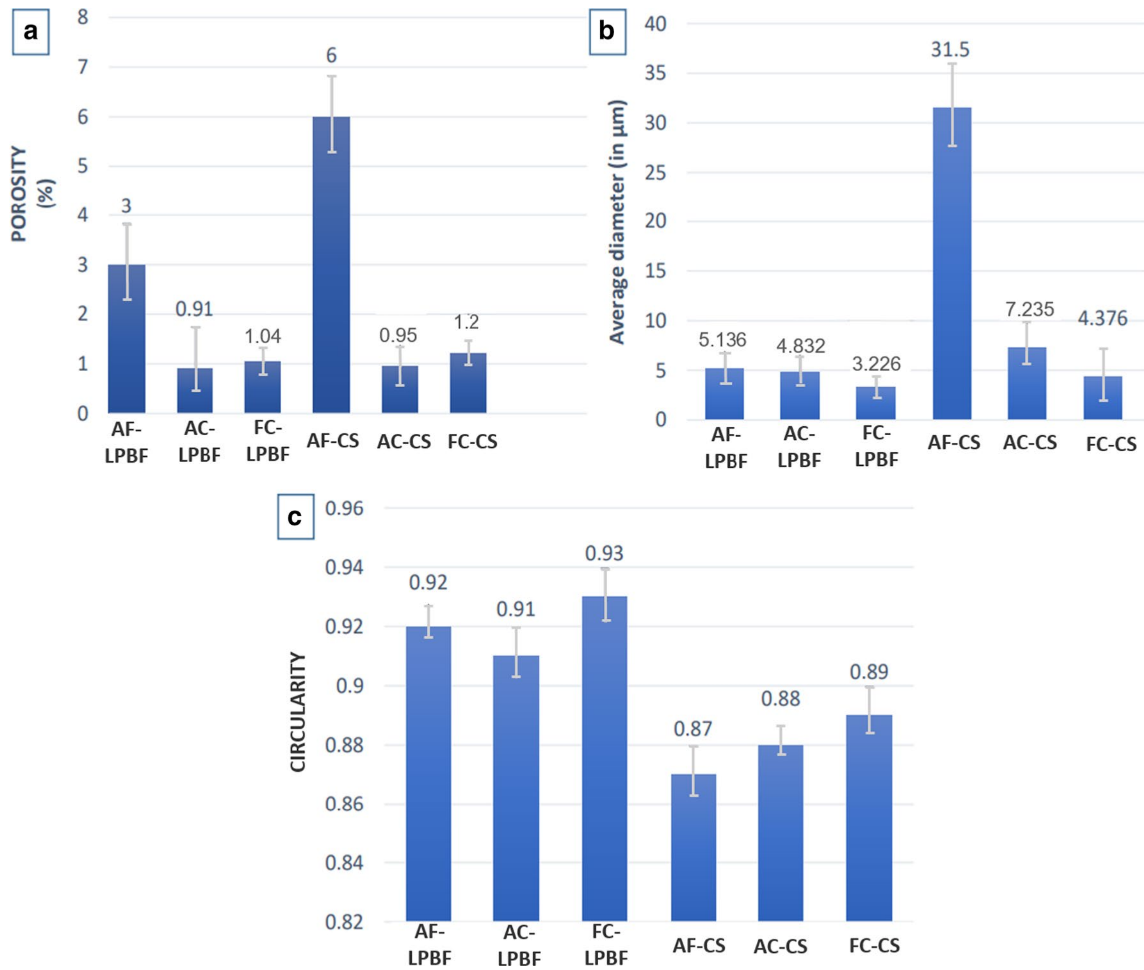

Fig. 8 **a** Average apparent surface porosity data, average pore diameter **b** and circularity **c** for as-fabricated (AF), air-cooled (AC), furnace-cooled (FC) SS316L samples formed with laser powder bed fusion (LPBF) and cold spraying (CS) technique

CS samples, poorly bonded interfaces between deposited particles get healed via solid-state diffusion (as explained by Huang et al.), resulting in decreased porosity compared to as-fabricated [56]. Therefore, to illustrate the heat-treatment effects on porosity, the probable mechanism during the solid-state diffusion of cold sprayed samples is shown in Fig. 9. As reported in the literature, the presence of strong and weak bonds between the particles is a result of adiabatic shear instability [45, 56]. The type of bonds (either weak or strong) plays a decisive part in affecting the pore morphology in terms of size [45]. Owing to the process of heat-treatment, the surface area of contact as a consequence of

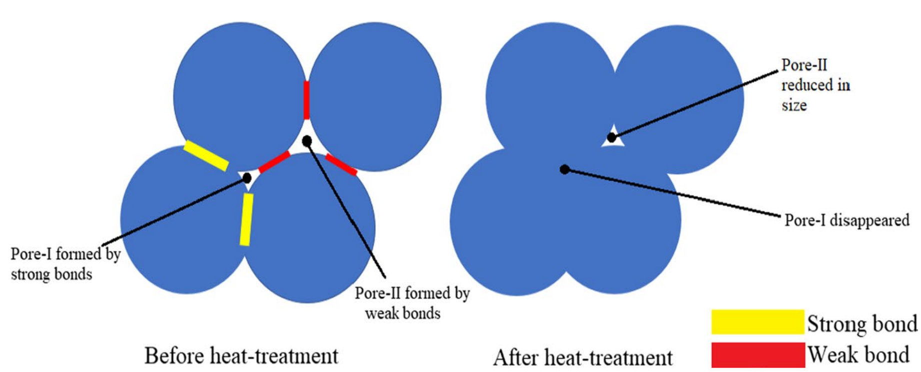

Fig. 9 The probable mechanism of pore disappearance and size reduction after heat treatment of the SS316L part fabricated using the process of cold spray (CS) technology

solid-state diffusion between particles (strongly and weakly bonded) increases, resulting in either pore disappearance (Pore-I disappeared) and reduction in pore size (Pore-II reduced in size) [57].

Moreover, higher porosity in FC-CS (1.2%) samples than AC-CS (0.95%) is an outcome of the recovery and recrystallization mechanism. Due to different annealing regimes followed, the equiaxed grains in FC-CS are 1.24 times larger than that of AC-CS owing to grain coarsening in the former case, as explained by Bandar AL-Mangour et al. [58], which results in more voids in FC-CS because of less packing efficiency. The observed porosity variation in AC- LPBF (0.91%) and FC- LPBF (1.04%) can also be ascribed to the same reason. The average diameters of pores formed in all the specimens are shown in Fig. 8b. The reduction in the pore diameter is noticed in post-processed samples, which concurs with the research conducted by Williams et al. [59]. Moreover, the AC- LPBF and AC-CS are observed to have a larger diameter in comparison with the respective FC-LPBF and FC-CS samples with almost the same %age porosity. It can be ascribed to the higher rate of cooling in air, which increases the pore diameter at the expense of decreasing pore quantity compared to the lower-cooling rate (furnace cooling). The presence of large diameter pores can be easily seen in the optical microstructures of air-cooled specimens (Fig. 7e, f), which further confirms the previously said statement.

As per the literature, the size of pores in implants can significantly affect the adhesion capability of cells inside the body [60, 61]. If holes are too tiny, cells are unable to move toward the center of the structure, hence impeding the passage of nutrients. On the other hand, if pores are too big, the effective specific surface area decreases, inhibiting cell adhesion. Therefore, the pore size must be within the ideal range for maximizing cell adhesion. The minimum pore size necessary for blood vessel formation is roughly 30 to 40 μm to facilitate metabolic component exchange and cell entry [62, 63]. The pore size of AF-CS is well within the specified range and may thus be regarded as favorable for biological applications compared to LPBF and post-treated samples.

From the circularity graph shown in Fig. 8c), it is concluded that the pores formed in AF-LPBF are closer to a perfect circular shape with a value of 0.92, contrary to AF-CS with a value of 0.87. The higher circularity in AF-LPBF is perhaps a consequence of its formation due to gas entrapment, whereas lesser in AF-CS may be owing to the lack of fusion due to the feedstock's plastic deformation resulting in an irregular-shaped cavity. The circularity of post-heat-treated samples slightly differs from that of the respective as-fabricated samples. This finding supports prior study published in the literature by Maskery et al. [64]. Kumar et al. [65] explored types of residual stress and associated type-III residual stresses with the porosity. After that, Zhang et al. [66], in their study, inversely related the circularity with residual stress present around the pore edges. Therefore, annealing treatment undergone in FC-LPBF and FC-CS has resulted in the highest circularity, which can be attributed to the removal of type-III residual stress produced owing to the non-uniform plastic deformation [67] in CS and rapid solidification of molten pool in LPBF [68, 69]. This claim is supported by the FWHM graph shown in Fig. 6c. The removal of such stresses is often influenced by the cooling rate, as verified by Neves et al. [70] and Hiremath et al. [71]. Less circularity of pores in AC-LPBF and AC-CS than in furnace-cooled specimens is because of the higher cooling rate in the former specimens resulting in more type-III residual stress.

It has been observed that material with a high porosity may not only prevent the stress shielding impact but also increase the bone in-growth efficiency [72]. Further, when the pore shape of the sample is comparable to the trabecular bone, especially in an irregular form, it may enhance the material's mechanical qualities and promote the proliferation of bone cells. As validated in the literature by Wang et al. [73], the irregular pore shape of AF-CS shown in the current investigation may contribute to enhanced cell growth over the implant in contrast to LPBF samples in both AF and HT states. In addition, the circularity of CS samples did not alter significantly due to heat treatment. However, as far as size and shape are concerned, the AF-CS sample can exhibit a favorable effect on the biological response.

3.4 Microstructure

Figures 10 and 11 show the etched microstructure of the top surface and the magnified view of LPBF and CS specimens in both as-formed and heat-treated state, respectively. The grain structures of the CS and LPBF samples are significantly different. The austenitic microstructure of AF-LPBF (Fig. 10a, b) consists of the two types of cellular sub-grains within the boundaries known as melt pool boundaries. One emerged as polygon-shaped, while the other appeared in elongated form, both orientated in the line of the highest thermal gradient. It is identical to the research conducted by Yusuf et al. [74] and Chen et al. [75]. According to Wang et al. [76], the rapid cooling of the melt-pool hinders the creation of secondary dendrite arms, leading to the formation of cellular sub-grains (Fig. 11). Moreover, as shown in Fig. 11a, the slightly bigger cellular subgrains are attributed to the slower cooling rate than the smaller grains. As per the study by [77], the columnar grain structures are evident along the build direction, having a length approximately equal to 1 mm. Also, as discussed earlier regarding the appearance of polygonal and elongated cellular structures from Fig. 10a, the combination of the columnar in build direction and cellular subgrains in the transverse direction

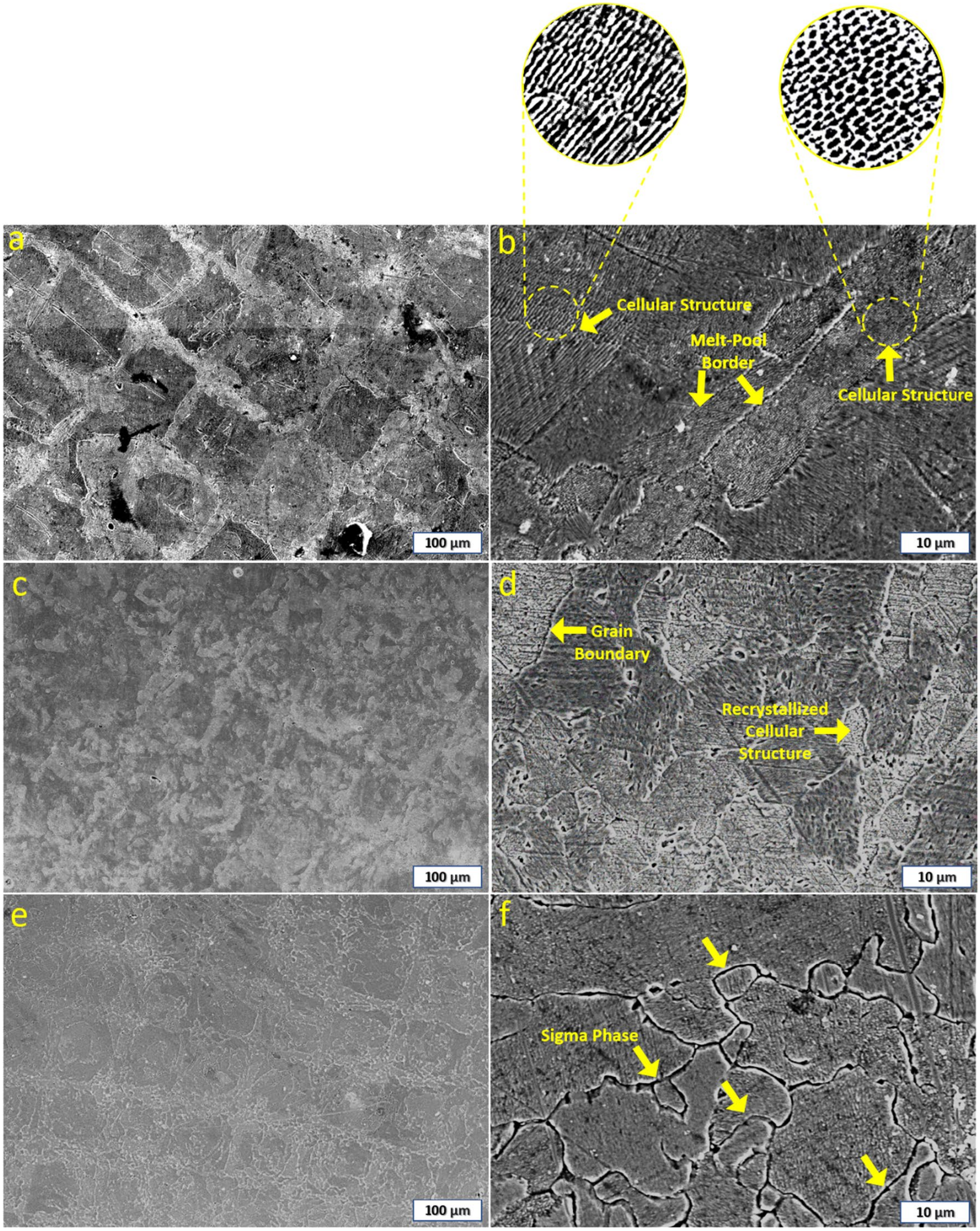

Fig. 10 Etched cross-sectional SEM images of laser powder bed fusion (LPBF) made SS316L sample, **a** as-fabricated (AF), **c** air-cooled (AC), **e** furnace-cooled (FC) along with its magnified view in **b**, **d** and **f**, respectively

is approximated as quadrilateral 3d substructure in various studies [78, 79].

The material composition inside the sub-grains of AF-LPBF is assessed using EDS point analysis at the grain boundary of cellular structure (1) As well as in the dark phase (2). The dark phase is attributed to the austenite, which is confirmed using XRD and EDS (Fig. 11b), showing less iron content. Moreover, the grain boundary (1) shows greater Mo (2.36%) and Cr (18%) content when compared with the austenite phase. The results are in accordance with

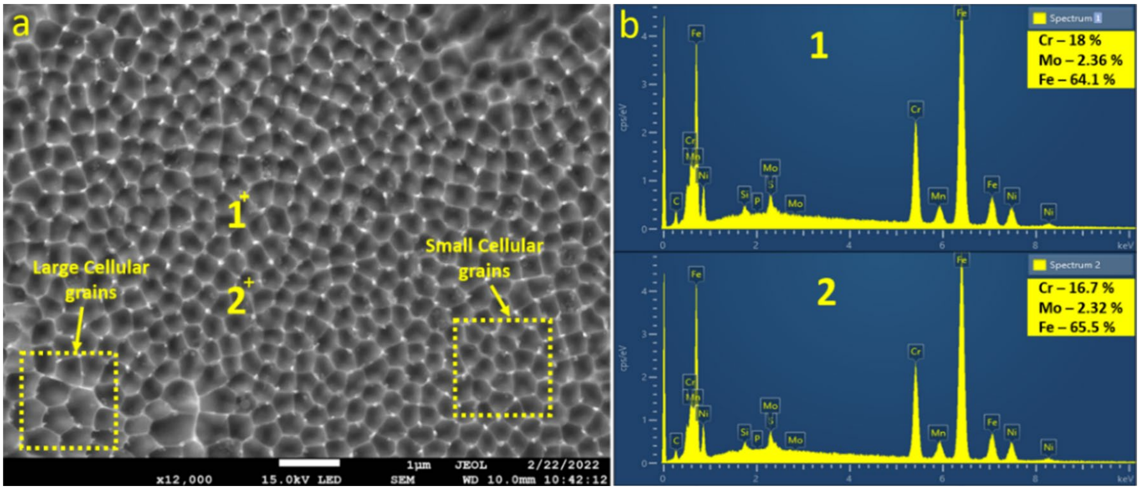

Fig. 11 **a** Etched cross-sectional magnified SEM image of as-fabricated (AF) laser powder bed fusion (LPBF) made SS316L sample along with the compositional analysis performed using energy-dispersive spectroscopy (EDS)

the research conducted by Saeidi et al. [80] on these sub-grains. They revealed that the boundaries of cellular sub-grains consist of excess alloying elements like Mo and Cr. This may be because during the phase change from liquid to solid, the solidification transports an excess quantity of Cr and Mo toward the end of the boundary. As a result, the LPBF-produced SS316L is likely to exhibit worse corrosion resistance than its cast-metal equivalent as an outcome of this elemental segregation [81]. In addition, the Marangoni effect causes oxides and other slight inclusions to be pushed to the melt pool's border. These inclusion flaws are quickly corroded because of the significant potential difference between them and the surrounding substrates. Moreover, in the study by Wang et al. [82], it has been found that the cell walls are decorated with a higher density of dislocations. During L-PBF processes, the wall thickness of the cell boundaries is reported to be related to solidification variables, such as temperature gradient, cooling rate, and solidification forward speed. Besides, the melt-pool border, basically formed by the fusion of two solidification fronts, is observed in the microstructure shown in Fig. 10a,b) [76, 83, 84].

In comparison with AF-LPBF, AF-CS microstructure consists of multi-crystalline grains and inter-particle interfaces. As per numerous studies made in the recent past, the same microstructure was detected and appeared similar to the original etched SS316L powder feedstock [58, 85, 86]. The carrier gas temperature of 873 K was employed to accelerate the particles rather than heat them. Moreover, the study by Schmidt et al. [87] shows that the inflight time of the powder particle with carrier gas is almost negligible, resulting in minimal particle temperature change. Attributed to the less particle temperature change, insignificant phase change occurred in the AF-CS part, resulting in a microstructure similar to feedstock in the central region (Fig. 12a,b). The multi-grains in the neighborhood of inter-particle interfaces exhibit severe plastic deformation, which must be due to the obvious reasons of the high-velocity impact of the particle on a substrate [37, 88, 89]. Moreover, in the vicinity of the inter-particle interface, the instantaneous heat is generated as a consequence of particle impact and adiabatic shear instability, followed by a small phase change [90]. The inter-particle interfaces (Fig. 12a,b) formed as a result of poor interfacial strength due to poor atomic diffusion among different particles in the cold spray process [91].

A magnified view of AF-LPBF in Fig. 10b indicates the presence of two types of cellular sub-grains having a size range of 0.25–0.4 µm in contrast to which multi-crystalline grains in AF-CS are in size range of 2.5–3 µm. Further, the microstructures of post-heat-treated LPBF samples (Fig. 10-c,d,e,f) are analyzed, which are significantly different from their as-fabricated counterpart (AF-LPBF). The subsequent recrystallization due to heat-treatment results in the atomic diffusion of the cellular sub-grains and dendritic structure in both the AC-LPBF (Fig. 10c,d) and FC-LPBF (Fig. 10e,f) samples.

Although the microstructures of AC-LPBF and FC-LPBF look similar at 100 µm magnification, the micrographs magnified views show the presence of sigma-phase in FC-LPBF (Fig. 10f), which is not observed in AC-LPBF (Fig. 10d). Sigma phase formed in the furnace-cooled specimen is composed of chromium and molybdenum, which is analyzed using EDS scan analysis as shown in Fig. 13. In their study, Hsieh et al. [57] ascertained the presence of the sigma phase and related its existence to the significant chromium content in SS316L material. Moreover, they provide information regarding the precipitation of the sigma phase in the region with a large chromium percentage. One of the

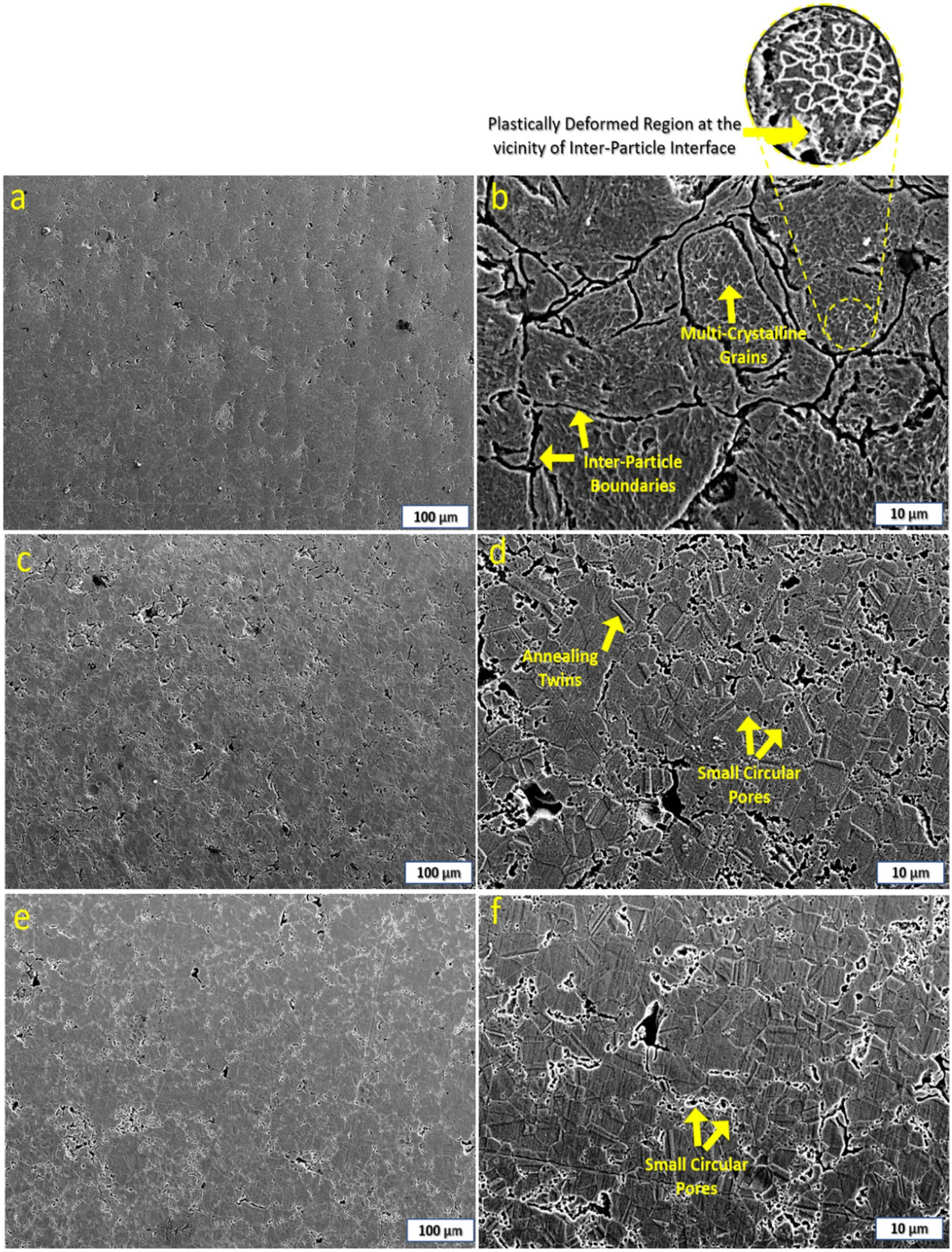

Fig. 12 Etched cross-sectional SEM images of cold-sprayed (CS) SS316L sample, **a** as-fabricated (AF), **c** air-cooled (AC), (e) furnace-cooled (FC) along with its magnified view in **b**, **d** and **f**, respectively

primary causes for the loss of SS316L properties, such as resistance to corrosion, and weldability, is the formation of the sigma phase, which is often found in different series of SS [92]. When the Cr concentration in SS exceeds a threshold (over 17% by weight), it is difficult to prevent this phase from precipitating [93]. Moreover, the introduction of

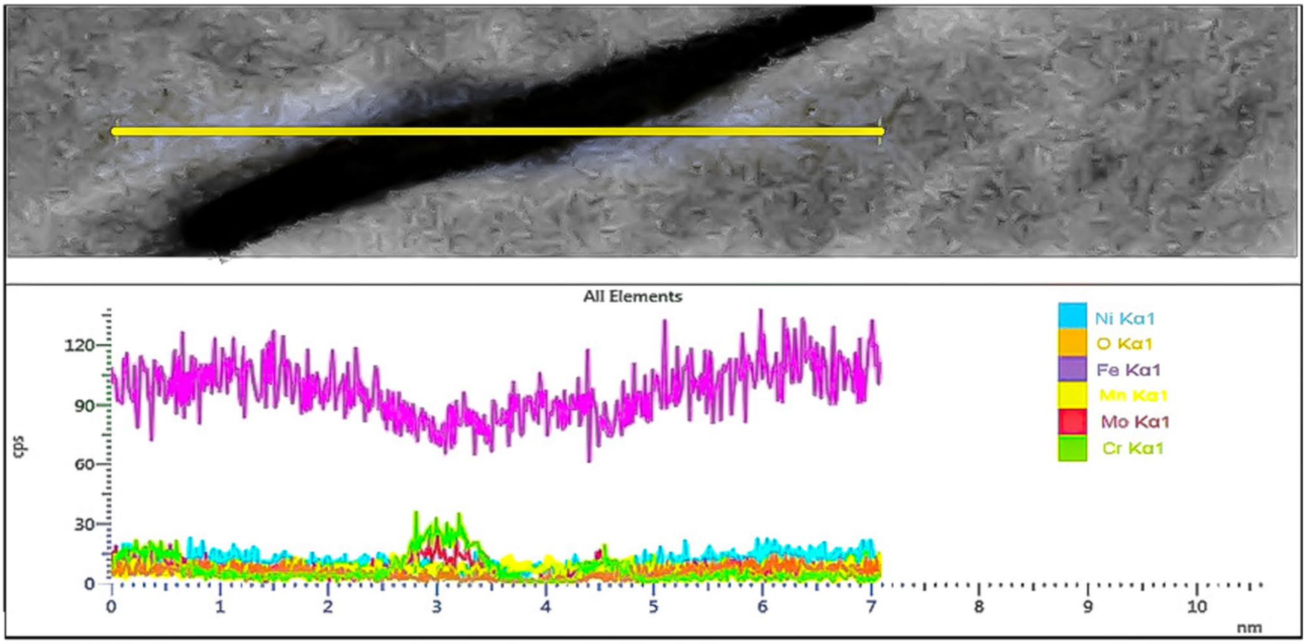

Fig. 13 Line scan analysis of sigma-phase formed in furnace cooled (FC) SS316L sample 3D printed with laser powder bed fusion (LPBF) technique

a significant ferrite stabilizer to SS316L (Cr, Si, or Mo) causes the phase to develop quickly. As per the different studies made in the past, the sigma phase generally transforms from the delta-ferrite [94]. However, in the present study, the sigma phase transforms out of the austenite, and the result is in accordance with the study made by Lewis [95]. Although the precipitation speed of the sigma phase-out of the austenite phase is prolonged compared to delta-ferrite, it is still possible if the temperature is greater than 1000 °C [96]. Furthermore, as per the research by Yin et al. [97], its presence is also observed in the LPBF fabricated SS316L samples when heat treated at 800 °C. According to the published research, the samples' cooling rate during heat treatment substantially affects the precipitation of the sigma phase. With a cooling rate of less than 0.1 °C/s, its existence becomes evident [94]. Therefore, in the present study, this formation may also be attributed to the slow cooling of the specimen from the temperature of 1100 °C [97] inside the furnace with a cooling rate of less than 0.1 °C/s.

Post-heat treatment of CS samples results in a remarkable difference compared to the as-fabricated samples (Fig. 12c, d, e, f). After heat treatment, recrystallization of inter-particle interfaces (formed due to improper particle–particle bonding) in AF-CS gets transformed into small pores, as shown in the magnified image of AC-CS (Fig. 12d).

and FC-CS (Fig. 12f). Numerous reports in the literature confirmed this observation [58, 98, 99]. Removal of inter-particle interfaces can be attributed to the process of atomic diffusion occurring during recrystallization. Both AC-CS and FC-CS recrystallize to form equiaxed grain structure and annealing twins with a size of 8.5 and 10.5 µm, respectively. The heat treatment strongly affects the presence of annealing twins in cold-sprayed microstructure [100]. The development of this type of microstructure is only possible when the specimen is heat treated above 1000 °C. Since the temperature in the present study is 1100 °C, the presence of twins was evident. Its formation can be attributed to the recovery and recrystallization of the distorted structure which may have formed owing to the plastic deformation of the high-velocity particle.

3.5 Mechanical properties

The microhardness variation in both LPBF and CS samples in as-fabricated and post-processed conditions is shown in Fig. 14. AF-CS sample with a grain size of 2.5–3 µm is observed to have 51.5% superior average hardness than its corresponding LPBF sample (grain size of 0.25–4 µm), with an absolute difference of 120.2 Hv. This might be because cold spraying causes strain hardening as a result of the plastic deformation caused by high-velocity particles impacting the substrate [85]. Even if the grain size is smaller in AF-LPBF, the effect of cold working makes the cold-sprayed specimen harder than the LPBF specimen. It is observed from the graph that the average hardness in the case of LPBF samples got increased after heat treatment. This increment in the hardness of AC-LPBF and FC-LPBF may be due to the significant reduction in porosity, as discussed earlier. The

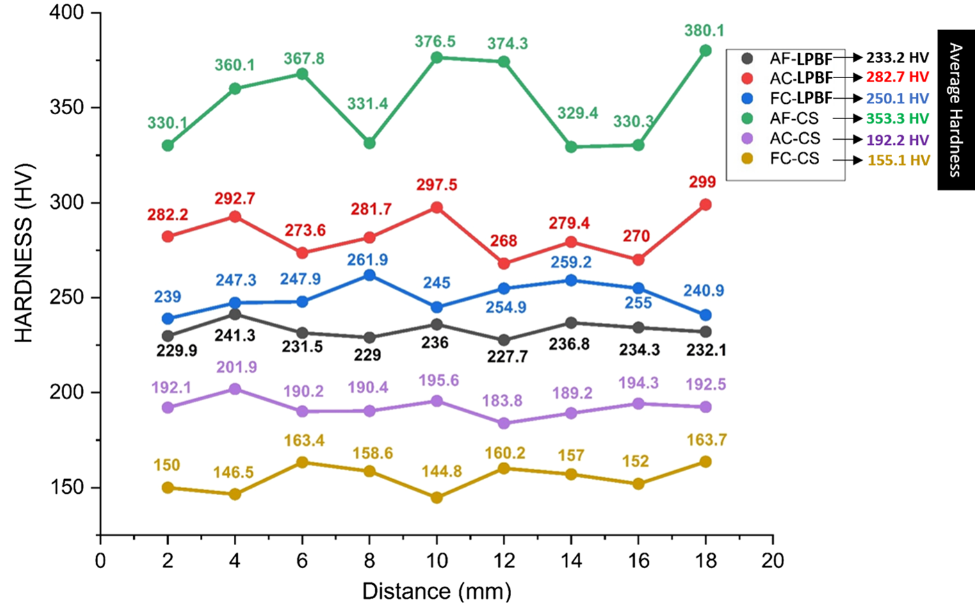

Fig. 14 Line graph showing the variation of microhardness (Hv) with a distance of as-fabricated (AF), air-cooled (AC), furnace-cooled (FC) SS316L specimens 3D printed with laser powder bed fusion (LPBF) and cold spraying (CS) techniques

observation is in accordance with the research carried out by Cherry et al. [14], Sun et al. [101] and Tucho et al. [102], in which they concluded that the high density or low porosity of the part results in the greater specimen microhardness. The increase in the mean hardness value of AC-LPBF in contrast to FC-LPBF with an absolute variation of 32.5 Hv was observed. Porosity variation being 0.13% has an insignificant influence on microhardness, according to the study conducted by Yusuf et al. [74]. Therefore, this rise in the hardness of air-cooled specimen (AC-LPBF) can be ascribed mainly to the grain refinement (grain size of 7.6 µm in AC-LPBF and 15 µm in FC-LPBF) owing to the high cooling rate (Fig. 10c). Moreover, the variation of microhardness along the distance in AF-LPBF and post-heat-treated samples is insignificant.

On the other hand, AC-CS and FC-CS samples experienced a decline in hardness compared to AF-CS with the value of 192.2 Hv and 155.1 Hv, respectively. Similar results have also been reported by Yin et al. [85] and Sundararajan et al. [100]. It is pertinent to mention that despite a significant decrease in the porosity of heat-treated CS samples, their hardness is decreased, contrary to LPBF cases. The reduction observed is mainly due to tempering, elimination of cold work effects and subsequent recrystallization. Moreover, the recrystallization of samples results in eradicating dislocations along with the emergence of grains in the form of annealing twins (Fig. 12d,f) [103]. The observed hardness difference between AC-CS and FC-CS cases may be due to the difference in cooling rates employed during heat treatment. As per the ImageJ analysis, the equiaxed grain of FC-CS is 10.5 µm, which is 1.24 times larger than that of AC-CS, resulting in the latter being harder, as per the famous Hall–Petch correlation. Further, owing to the non-uniform plastic deformation, the difference of hardness along the distance is quite significant in AF-CS [100]**.** Despite of noteworthy variability in AF-CS, the thermal treatment of the same tends to reduce the difference to the greater extent as shown in AC-CS and FC-CS graph. This can be attributed to the process of stress relief occurred over the surface on account of heat-treatment process.

In addition to hardness data, the elastic modulus of all samples is evaluated using the indentation method (Fig. 15). The elastic modulus values for LPBF samples are substantially greater than those for CS samples (Fig. 15b). In particular, the LPBF sample in its AF state has Young's modulus of 184.55 GPa, which is around 66.5 GPa greater than the AF-CS part. The AF-LPBF modulus value is consistent with prior research by Merkt et al. [104] and Yadroitsev et al. [105], who observed values ranging from 140 to 220 GPa. On the other hand, heat treatment has significantly altered the modulus values of LPBF samples. The FC-LPBF and AC-LPBF have a value of 242.5 and 296.6 GPa, respectively. This evident increase in the value can be attributed to the reduction of porosity values mentioned earlier in this study. Also, as per the study by Jouget et al. [106], the elastic modulus of LPBF fabricated cobalt alloy tends to show an inverse relationship with porosity. Therefore, these results from the literature are in agreement with the present study. Moreover, aside from porosity, the greater dislocation density and previously reported segregation effect (Fig. 11) in AF-LPBF must also be taken into consideration while analyzing the material's Young's modulus in contrast to FC and AC-LPBF. The segregation region in the cellular structure of AF-LPBF consists of excess Cr and Mo constituents with high dislocation density. According to the research by

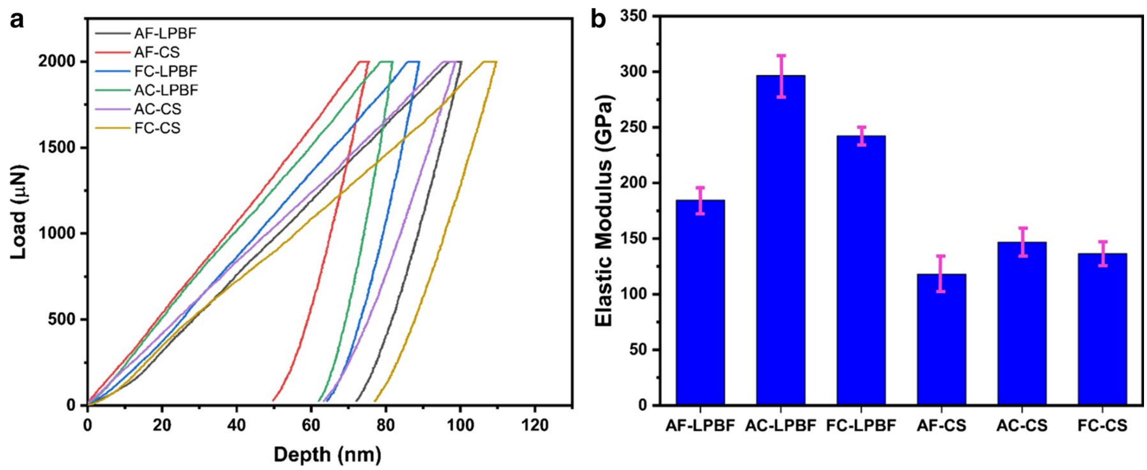

Fig. 15 **a** Load vs. displacement curve and **b** bar graph of all the samples with their respective designation prepared using laser powder bed fusion (LPBF) and cold spraying (CS) techniques

Benito et al. [107], the presence of dislocation densities has affected the Young's modulus values in the negative sense. Therefore, the occurrence of the same in the case of AF-LPBF also accounts for the reduction in modulus values when compared with heat-treated samples. Despite the fact that the modulus value in LPBF is low when compared to heat-treated samples, the stress shielding effect in AF-LPBF-made implant will be discernible, which may deteriorate bone strength.

On the other hand, AF-CS exhibited the lowest modulus value of 118 GPa when compared with LPBF samples. This least value is ascribed to the high porosity and presence of significant inter-particle boundaries between different splats (Fig. 12b). This particular reason is made in light of the study by Sundarajan et al. [100], who studied the effect of interparticle boundaries in AF-CS on Young's modulus. Post-heat-treated samples revealed a 24 and 15% hike in elastic modulus of AC-CS and FC-CS compared to AF-CS. This increase is due to the intersplat boundary diffusion during heat treatment (Fig. 12d, f), resulting in the reduced porosity and hence, greater Young's modulus. Moreover, ductility in implants is well known to be essential for implant contouring and shape [108]. However, it is important to note that the AF-CS samples are highly brittle, and the ductility is greatly enhanced following heat treatment, as indicated in Fig. 15a. Although the elastic modulus of the AF-CS sample is the least among all the samples representing its ability to reduce the stress shielding effect, its inherent brittle behavior due to strain hardening is undesirable for orthopedic applications. Therefore, with the good ductile properties indicated in the graph and just a 15% greater elastic modulus value, which is insignificant, the FC-CS sample can be considered acceptable for use in sbiomedical applications.

4 Conclusions

Laser powder bed fusion (LPBF) and cold spray (CS) techniques were successfully used to print SS316L samples. The high value of surface roughness in AF-CS before finishing operations indicates good signs of improved biocompatibility at the investigated parameters. Moreover, after the finishing and polishing step, AF-CS samples were found to have higher porosity than their LPBF printed counterparts. The irregular morphology and optimum size of pores in AF-CS may result in better cell proliferation as suggested by literature. Moreover, porosity was found to reduce by heat treatment in both cases. Distinct microstructure (equiaxed grains with annealing twins) was observed in both FC-CS and AC-CS samples. In the case of heat-treated LPBF cases, slow cooling in the furnace led to the formation of a sigma phase, which distinguishes it from the air-cooled case. Heat treatment enhanced the hardness of the LPBF printed samples, whereas it decreased the hardness in the case of CS printed samples. The improved hardness in the former case was attributed to the reduced porosity values, whereas the reduction in the latter case owing to the elimination of cold work effects. The hardness value of FC-CS (155 Hv) being the least suggests that heat treatment followed by furnace cooling could be an appropriate approach to reduce mechanical strength mismatch between SS 316 L steel and bone for orthopedic applications. Even though the AF-CS sample has the lowest elastic modulus with greater porosity among all the samples, its intrinsic brittleness owing to strain hardening is unsuitable for orthopedic applications. As a result, the FC-CS sample may be used in biomedical applications due to its strong, ductile characteristics and a little higher elastic modulus value in contrast to AF-CS. Hence, this study opens a pathway to explore cold spray as a viable technique to manufacture bio-implants with tailor-made porosity and hardness by optimizing various process parameters.

Declarations

Conflict of interest The authors declare that there is no conflict of interest.

Ethical approval This article does not contain any studies with human or animal subjects performed by any of the authors.

Consent to participate The consent of all authors has been obtained.

Consent for publication The consent of all authors has been obtained.

References

1. Jha R, Dulikravich GS (2021) Discovery of new Ti-Based alloys aimed at Avoiding/Minimizing formation of α” and ω-phase using CALPHAD and artificial intelligence. Metals (Basel) 11(1):15. https://doi.org/10.3390/met11010015
2. Jeong W, Shin SE, Choi H (2020) Microstructure and mechanical properties of titanium–equine bone biocomposites. Metals (Basel) 10(5):1–10. https://doi.org/10.3390/met10050581
3. Singh A, Singh H (2022) Metal additive manufacturing: from history to applications. In: Khan MA, Jappes JTW (eds) Springer International Publishing. Cham, pp 3–32. https://doi.org/10.1007/978-3-030-89401-6_1
4. Kozak J, Zakrzewski T, Witt M, Dębowska-Wąsak M (2021) Selected problems of additive manufacturing using SLS/SLM processes. Trans Aerosp Res 2021(1):24–44. https://doi.org/10.2478/tar-2021-0003
5. Lykov PA, Safonov EV, Akhmedianov AM (2016) Selective laser melting of copper. Mater Sci Forum 843:284–288. https://doi.org/10.4028/www.scientific.net/MSF.843.284
6. Ni J et al (2019) “Three-dimensional printing of metals for biomedical applications. Mater Today Bio 3:100024. https://doi.org/10.1016/j.mtbio.2019.100024
7. Sing SL, Tey CF, Tan JHK, Huang S, Yeong WY (2020) 3D printing of metals in rapid prototyping of biomaterials techniques in additive manufacturing. In: Narayan R (ed) Rapid prototyping of biomaterials. Woodhead Publishing, pp 17–40
8. Huiskes R, Weinans H, van Rietbergen B (1992) The relationship between stress shielding and bone resorption around total hip stems and the effects of flexible materials. Clin Orthop Relat Res 274:124–134
9. Li W, Cao C, Yin S (2020) Solid-state cold spraying of Ti and its alloys: a literature review. Prog Mater Sci 110:100633. https://doi.org/10.1016/j.pmatsci.2019.100633
10. Champagne VK, Champagne VK, Widener C (2017) Cold spray applications. In: Cavaliere Pasquale (ed) Cold-Spray Coatings: Recent Trends and Future perspectives. Springer International Publishing, Cham
11. Sakaki K (2004) Cold spray process ~ overview and application trends ~. Mater Sci Forum 449–452:1305–1308. https://doi.org/10.4028/www.scientific.net/msf.449-452.1305
12. Wu W-W et al (2019) Bone hardness of different anatomical regions of human radius and its impact on the pullout strength of screws. Orthop Surg 11(2):270–276. https://doi.org/10.1111/os.12436
13. Attar H, Calin M, Zhang LC, Scudino S, Eckert J (2014) Manufacture by selective laser melting and mechanical behavior of commercially pure titanium. Mater Sci Eng A 593:170–177. https://doi.org/10.1016/j.msea.2013.11.038
14. Cherry JA, Davies HM, Mehmood S, Lavery NP, Brown SGR, Sienz J (2014) Investigation into the effect of process parameters on microstructural and physical properties of 316L stainless steel parts by selective laser melting. Int J Adv Manuf Technol 76(5–8):869–879. https://doi.org/10.1007/s00170-014-6297-2
15. Li H, Ramezani M, Li M, Ma C, Wang J (2018) Effect of process parameters on tribological performance of 316L stainless steel parts fabricated by selective laser melting. Manuf Lett 16:36–39. https://doi.org/10.1016/j.mfglet.2018.04.003
16. Kong D et al (2019) Mechanical properties and corrosion behavior of selective laser melted 316L stainless steel after different heat-treatment processes. J Mater Sci Technol 35(7):1499–1507. https://doi.org/10.1016/j.jmst.2019.03.003
17. Liu J et al (2020) Effect of scanning speed on the microstructure and mechanical behavior of 316L stainless steel fabricated by selective laser melting. Mater Design 186:108355. https://doi.org/10.1016/j.matdes.2019.108355
18. Bedmar J, Riquelme A, Rodrigo P, Torres B, Rams J (2021) Comparison of different additive manufacturing methods for 316l stainless steel. Materials 14(21):6504. https://doi.org/10.3390/ma14216504
19. Raffa ML, Nguyen VH, Hernigou P, Flouzat-Lachaniette CH, Haiat G (2021) Stress shielding at the bone-implant interface: influence of surface roughness and of the bone-implant contact ratio. J Orthop Res 39(6):1174–1183. https://doi.org/10.1002/jor.24840
20. Middleton KA, Ma YH, You L (2017) Measuring bone cell response to fluid shear stress and hydrostatic/dynamic pressure. In: Zdero RBT-EMOB (ed) Experimental Methods in Orthopaedic Biomechanic. Elsevier, UK, pp 217–232. https://doi.org/10.1016/B978-0-12-803802-4.00014-7
21. Röttger A et al (2020) Microstructure and mechanical properties of 316L austenitic stainless steel processed by different SLM devices. Int J Adv Manuf Technol 108(3):769–783. https://doi.org/10.1007/s00170-020-05371-1
22. Ahmed Obeidi M et al (2021) Comparison of the porosity and mechanical performance of 316L stainless steel manufactured on different laser powder bed fusion metal additive manufacturing machines. J Mater Res Technol 13:2361–2374. https://doi.org/10.1016/j.jmrt.2021.06.027
23. Do Jung H et al (2014) Highly aligned porous Ti scaffold coated with bone morphogenetic protein-loaded silica/chitosan hybrid for enhanced bone regeneration. J Biomed Mater Res - Part B Appl Biomater 102(5):913–921. https://doi.org/10.1002/jbm.b.33072
24. Bari K, Arjunan A (2019) Extra low interstitial titanium based fully porous morphological bone scaffolds manufactured using selective laser melting. J Mech Behav Biomed Mater 95:1–12. https://doi.org/10.1016/j.jmbbm.2019.03.025
25. Li L, Crosby K, Sawicki M (2012) Effects of surface roughness of hydroxyapatite on cell attachment and proliferation. J Biotechnol Biomater. https://doi.org/10.4172/2155-952x.1000150
26. Wennerberg A (1999) The role of surface roughness for implant incorporation in bone. Cells Mater 9(1):1–19
27. Haslauer CM, Springer JC, Harrysson OLA, Loboa EG, Monteiro-Riviere NA, Marcellin-Little DJ (2010) In vitro biocompatibility of titanium alloy discs made using direct metal fabrication. Med Eng Phys 32(6):645–652. https://doi.org/10.1016/j.medengphy.2010.04.003
28. Martin JY et al (1995) Effect of titanium surface roughness on proliferation, differentiation, and protein synthesis of human

osteoblast-like cells (MG63). J Biomed Mater Res 29(3):389–401. https://doi.org/10.1002/jbm.820290314
29. S. Gulizia, (2016) Cold spray additive manufacturing : from the laboratory to the market. [Online]. Available: http://www.asminternational.org/documents/10192/26746001/20+-+Gulizia.pdf/b8edc449-2333-427d-a05b-84bd980eb1f4
30. Schmidt T, Gaertner F, Kreye H (2006) New developments in cold spray based on higher gas and particle temperatures. Proc Int Therm Spray Conf 15:488–494. https://doi.org/10.1361/105996306X147144
31. Widener CA, Ozdemir OC, Carter M (2018) Structural repair using cold spray technology for enhanced sustainability of high value assets. Procedia Manufacturing 21:361–368. https://doi.org/10.1016/j.promfg.2018.02.132
32. Zou Y (2021) Cold spray additive manufacturing: microstructure evolution and bonding features. Accounts Mater Res. https://doi.org/10.1021/accountsmr.1c00138
33. Spee3d, (2021) LightSpee3d 3d metal printer." https://www.spee3d.com/product/lightspee3d/ (accessed Oct. 09, 2021)
34. Titomic, (2021) TKF 9000: THE WORLD'S LARGEST and FASTEST." https://titomic.com/products-services/tkf-systems/ (accessed Jun. 24, 2021)
35. Majeed A, He J, Jiao L, Zhong X, Sheng Z (2015) Surface properties and biocompatibility of nanostructured TiO2 film deposited by RF magnetron sputtering. Nanoscale Res Lett 10(1):56. https://doi.org/10.1186/s11671-015-0732-7
36. Thomas M, Baxter GJ, Todd I (2016) Normalised model-based processing diagrams for additive layer manufacture of engineering alloys. Acta Mater 108:26–35. https://doi.org/10.1016/j.actamat.2016.02.025
37. Salman OO, Gammer C, Chaubey AK, Eckert J, Scudino S (2019) Effect of heat-treatment on microstructure and mechanical properties of 316L steel synthesized by selective laser melting. Mater Sci Eng A 748:205–212
38. ASM Handbook Volume 4A: Steel Heat Treating Fundamentals and Processes ASM Handbook Volume 4B: Steel Heat Treating Technologies ASM Handbook Volume 4C: Induction Heating and Heat-treatment ASM Handbook Volume 4D: Heat Treating of Irons and Steels, vol. 4
39. López MF, Gutiéerrez A, García-Alonso MC, Escudero ML (1998) Surface analysis of a heat-treated, Al-containing, iron-based superalloy. J Mater Res 13(12):3411–3416. https://doi.org/10.1557/JMR.1998.0464
40. Escudero ML, López MF, Ruiz J, García-Alonso MC, Canahua H (1996) Comparative study of the corrosion behavior of MA-956 and conventional metallic biomaterials. J Biomed Mater Res 31(3):313–317. https://doi.org/10.1002/(SICI)1097-4636(199607)31:3%3c313::AID-JBM4%3e3.0.CO;2-P
41. Gu D, Shen Y (2009) Balling phenomena in direct laser sintering of stainless steel powder: metallurgical mechanisms and control methods. Mater Des 30(8):2903–2910. https://doi.org/10.1016/j.matdes.2009.01.013
42. Grujicic M, Zhao CL, Derosset W, Helfritch D (2004) Adiabatic shear instability based mechanism for particle/substrate bonding in the cold-gas dynamic-spray process. Mater Des 25:681–688. https://doi.org/10.1016/j.matdes.2004.03.008
43. Bielousova O, Kocimski J, Maev RG, Smurov I, Scharff W, Leshchynsky V (2016) Localisation of deformation in cold gas dynamic spraying. Surf Eng 32(9):655–662. https://doi.org/10.1179/1743294415Y.0000000059
44. Palodhi L, Das B, Singh H (2021) Effect of particle size and morphology on critical velocity and deformation behavior in cold spraying. J Mater Eng Perform 30(11):8276–8288. https://doi.org/10.1007/s11665-021-05997-6
45. Assadi H, Gärtner F, Stoltenhoff T, Kreye H (2003) Bonding mechanism in cold gas spraying. Acta Mater 51(15):4379–4394. https://doi.org/10.1016/S1359-6454(03)00274-X
46. Walter R, Kannan MB (2011) Influence of surface roughness on the corrosion behaviour of magnesium alloy. Mater Des 32(4):2350–2354. https://doi.org/10.1016/j.matdes.2010.12.016
47. Okayasu M, Fukui H, Ohfuji H, Shiraishi T (2013) Strain-induced martensite formation in austenitic stainless steel. J Mater Sci 48(18):6157–6166. https://doi.org/10.1007/s10853-013-7412-8
48. Monrrabal G, Bautista A, Guzman S, Gutierrez C, Velasco F (2019) Influence of the cold working induced martensite on the electrochemical behavior of AISI 304 stainless steel surfaces. J Mater Res Technol 8(1):1335–1346. https://doi.org/10.1016/j.jmrt.2018.10.004
49. Chen AY et al (2011) The influence of strain rate on the microstructure transition of 304 stainless steel. Acta Mater 59(9):3697–3709. https://doi.org/10.1016/j.actamat.2011.03.005
50. Yin S, Cizek J, Yan X, Lupoi R (2019) Surface and Coatings Technology Annealing strategies for enhancing mechanical properties of additively manufactured 316L stainless steel deposited by cold spray. Surf Coat Technol 370:353–361. https://doi.org/10.1016/j.surfcoat.2019.04.012
51. Khairallah SA, Anderson AT, Rubenchik A, King WE (2016) Laser powder-bed fusion additive manufacturing: physics of complex melt flow and formation mechanisms of pores, spatter, and denudation zones. Acta Mater 108:36–45. https://doi.org/10.1016/j.actamat.2016.02.014
52. Sola A, Nouri A (2019) Microstructural porosity in additive manufacturing: The formation and detection of pores in metal parts fabricated by powder bed fusion. J Adv Manuf Process 1(3):1–21. https://doi.org/10.1002/amp2.10021
53. Zhang L et al (2016) Review on manufacture by selective laser melting and properties of titanium based materials for biomedical applications. Mater Technol. https://doi.org/10.1179/1753555715Y.0000000076
54. Trapp J, Rubenchik AM, Guss G, Matthews MJ (2017) In situ absorptivity measurements of metallic powders during laser powder-bed fusion additive manufacturing. Appl Mater Today 9:341–349. https://doi.org/10.1016/j.apmt.2017.08.006
55. Frostevarg J, Volpp J, Thompson C, Prasad HS, Fedina T, Brückner F (2019) Influence of the vapour channel on processing in laser powder bed fusion. Proc Manufact 36:80–87. https://doi.org/10.1016/j.promfg.2019.08.012
56. Huang J et al (2019) Influence of cold gas spray processing conditions on the properties of 316L stainless steel coatings. Surf Eng 35(9):784–791. https://doi.org/10.1080/02670844.2019.1584967
57. Zhou H et al (2019) Pores structure change induced by heat-treatment in Cold-Sprayed Ti6Al4V coating. J Therm Spray Technol 28(6):1199–1211. https://doi.org/10.1007/s11666-019-00882-0
58. Al-mangour B, Vo P, Mongrain R, Irissou E, Yue S (2014) Effect of heat-treatment on the microstructure and mechanical properties of stainless steel 316L coatings produced by cold spray for biomedical applications. ASM Int 23:641–652. https://doi.org/10.1007/s11666-013-0053-2
59. Tammas-Williams S, Withers PJ, Todd I, Prangnell PB (2016) Porosity regrowth during heat-treatment of hot isostatically pressed additively manufactured titanium components. Scr Mater 122:72–76. https://doi.org/10.1016/j.scriptamat.2016.05.002
60. Loh QL, Choong C (2012) Three-dimensional Scaffolds for Tissue Engineering Applications: role of porosity and pore size. Tissue Eng Part B Rev 3:1–61
61. 2013 Dien et al. and 2013 Sheean et al., (2008) Effect of Pore Size on the Physicochemical Properties and Osteogenesis of Ti6Al4V Porous Scaffolds with Bionic Structure. *Bone*, 23(1): 1–7, https://doi.org/10.1002/smll.201000544.Uniform.

62. Madden LR et al (2010) Proangiogenic scaffolds as functional templates for cardiac tissue engineering. Proc Natl Acad Sci USA 107(34):15211–15216. https://doi.org/10.1073/pnas.1006442107
63. Oliviero O, Ventre M, Netti PA (2012) Functional porous hydrogels to study angiogenesis under the effect of controlled release of vascular endothelial growth factor. Acta Biomater 8(9):3294–3301. https://doi.org/10.1016/j.actbio.2012.05.019
64. Maskery I et al (2016) Quantification and characterisation of porosity in selectively laser melted Al-Si10-Mg using X-ray computed tomography. Mater Charact 111:193–204
65. N. Kumar, R. S. Mishra, and J. A. Baumann, (2014) Introduction. In: *Residual Stresses in Friction Stir Welding*, pp. 1–4. doi: https://doi.org/10.1016/b978-0-12-800150-9.00001-7
66. Zhang P, Zuo Y (2019) Relationship between porosity, pore parameters and properties of microarc oxidation film on AZ91D magnesium alloy. Results Phys 12(January):2044–2054. https://doi.org/10.1016/j.rinp.2019.01.095
67. Shayegan G et al (2014) Residual stress induced by cold spray coating of magnesium AZ31B extrusion. J Mater 60:72–84. https://doi.org/10.1016/j.matdes.2014.03.054
68. Ali H, Ghadbeigi H, Mumtaz K (2018) Residual stress development in selective laser-melted Ti6Al4V: a parametric thermal modelling approach. Int J Adv Manuf Technol 97(5–8):2621–2633. https://doi.org/10.1007/s00170-018-2104-9
69. Mercelis P, Kruth JP (2006) Residual stresses in selective laser sintering and selective laser melting. Rapid Prototyp J 12(5):254–265. https://doi.org/10.1108/13552540610707013
70. Neves FO, Oliviera TLL, Braga DU, Da Silva ASC (2014) Influence of heat-treatment on residual stress in cold-forged parts. Adv Mater Sci Eng 2014:1–6. https://doi.org/10.1155/2014/658679
71. Hiremath P, Sharma S, Gowrishankar MC, Shettar M, Gurumurthy BM (2020) Effect of post carburizing treatments on residual stress distribution in plain carbon and alloy steels – a numerical analysis. J Mater Res Technol 9(4):439–8450. https://doi.org/10.1016/j.jmrt.2020.05.104
72. Karageorgiou V, Kaplan D (2005) Porosity of 3D biomaterial scaffolds and osteogenesis. Biomaterials 26(27):5474–5491. https://doi.org/10.1016/j.biomaterials.2005.02.002
73. Wang C et al (2020) Effect of pore size on the physicochemical properties and Osteogenesis of Ti6Al4V Porous Scaffolds with bionic structure. ACS Omega 5(44):28684–28692. https://doi.org/10.1021/acsomega.0c03824
74. Yusuf SM, Chen Y, Boardman R, Yang S, Gao N (2017) Investigation on porosity and microhardness of 316L stainless steel fabricated by selective laser melting. Metals (Basel) 7(2):1–12. https://doi.org/10.3390/met7020064
75. Chen W, Yin G, Feng Z, Liao X (2018) Effect of powder feedstock on microstructure and mechanical properties of the 316L stainless steel fabricated by selective laser melting. Metals 8(9):729. https://doi.org/10.3390/met8090729
76. Wang D, Song C, Yang Y, Bai Y (2016) Investigation of crystal growth mechanism during selective laser melting and mechanical property characterization of 316L stainless steel parts. Mater Des 100:291–299. https://doi.org/10.1016/j.matdes.2016.03.111
77. Leicht A, Yu CH, Luzin V, Klement U, Hryha E (2020) Effect of scan rotation on the microstructure development and mechanical properties of 316L parts produced by laser powder bed fusion. Mater Charact 163(March):2–10. https://doi.org/10.1016/j.matchar.2020.110309
78. O. Zinovieva and A. Zinoviev, (2019) *Numerical analysis of the grain morphology and texture in 316L steel produced by selective laser melting*, vol. 2167. doi: https://doi.org/10.1063/1.5132274
79. Zhao C, Bai Y, Zhang Y, Wang X, Xue JM, Wang H (2021) Influence of scanning strategy and building direction on microstructure and corrosion behaviour of selective laser melted 316L stainless steel. Mater Des 209:109999. https://doi.org/10.1016/j.matdes.2021.109999
80. Saeidi K, Akhtar F (2018) Subgrain-controlled grain growth in the laser-melted 316 L promoting strength at high temperatures. R Soc Open Sci 5(5):141504. https://doi.org/10.1098/rsos.172394
81. Zhou C et al (2020) Enhanced corrosion resistance of additively Manufactured 316L stainless steel after heat-treatment. J Electrochem Soc 167(14):141504. https://doi.org/10.1149/1945-7111/abc10e
82. Wang YM et al (2018) Additively manufactured hierarchical stainless steels with high strength and ductility. Nat Mater 17(1):63–70. https://doi.org/10.1038/NMAT5021
83. Zhang B, Li Y, Bai Q (2017) Defect formation mechanisms in selective laser melting: a review. Chin J Mech Eng 30(3):515–527. https://doi.org/10.1007/s10033-017-0121-5
84. Shifeng W, Shuai L, Qingsong W, Yan C, Sheng Z, Yusheng S (2014) Effect of molten pool boundaries on the mechanical properties of selective laser melting parts. J Mater Process Technol 214(11):2660–2667. https://doi.org/10.1016/j.jmatprotec.2014.06.002
85. Yin S et al (2019) Hybrid additive manufacture of 316L stainless steel with cold spray and selective laser melting: Microstructure and mechanical properties. J Mater Process Technol 273:116248
86. Zhu Y, Peng T, Jia G, Zhang H, Xu S, Yang H (2019) Electrical energy consumption and mechanical properties of selective- laser-melting-produced 316L stainless steel samples using various processing parameters. J Clean Prod 208:77–85. https://doi.org/10.1016/j.jclepro.2018.10.109
87. Schmidt T, Gärtner F, Assadi H, Kreye H (2006) Development of a generalized parameter window for cold spray deposition. Acta Mater 54(3):729–742
88. Kim HJ, Lee CH, Hwang SY (2005) Fabrication of WC-Co coatings by cold spray deposition. Surf Coatings Technol 191(2–3):335–340. https://doi.org/10.1016/j.surfcoat.2004.04.058
89. Zou Y, Qin W, Irissou E, Legoux JG, Yue S, Szpunar JA (2009) Dynamic recrystallization in the particle/particle interfacial region of cold-sprayed nickel coating: Electron backscatter diffraction characterization. Scr Mater 61(9):899–902. https://doi.org/10.1016/j.scriptamat.2009.07.020
90. Lee C, Kim J (2015) Microstructure of kinetic spray coatings: a review. J Therm Spray Technol 24(4):592–610. https://doi.org/10.1007/s11666-015-0223-5
91. Sun W et al (2020) Post-process treatments on supersonic cold sprayed coatings: a review. Coatings 10(2):123. https://doi.org/10.3390/coatings10020123
92. A. Jarfors, (2014) Sigma phase in 316L and 304L. Sweden, 2004. [Online]. Available: http://inis.iaea.org/search/search.aspx?orig_q=RN:36083651
93. S. Astafurov and E. Astafurova, (2021) Phase composition of austenitic stainless steels in additive manufacturing : a review
94. Hsieh C-C, Wu W (2012) Overview of intermetallic sigma phase precipitation in stainless steels. ISRN Metall 2012(4):1–16. https://doi.org/10.5402/2012/732471
95. Lewis MH (1966) Precipitation of (Fe, Cr) sigma phase from austenite. Acta Metall 14(11):1421–1428. https://doi.org/10.1016/0001-6160(66)90162-3
96. Na YS, Park NK, Reed RC (2000) Sigma morphology and precipitation mechanism in udimet 720Li. Scr Mater 43(7):585–590. https://doi.org/10.1016/S1359-6462(00)00441-3
97. Yin H, Song M, Deng P, Li L, Prorok BC, Lou X (2021) Thermal stability and microstructural evolution of additively manufactured 316L stainless steel by laser powder bed fusion at 500–800 ℃. Addit Manuf 41(March):20–22. https://doi.org/10.1016/j.addma.2021.101981

98. Li WY et al (2007) Ti and Ti-6Al-4V coatings by cold spraying and microstructure modification by heat-treatment. Adv Eng Mater 9(5):418–423. https://doi.org/10.1002/adem.200700022
99. Zahiri SH, Fraser D, Jahedi M (2009) Recrystallization of cold spray-fabricated CP titanium structures. J Therm Spray Technol 18(1):16–22. https://doi.org/10.1007/s11666-008-9212-2
100. Sundararajan G, Phani PS, Jyothirmayi A, Gundakaram RC (2009) The influence of heat-treatment on the microstructural, mechanical and corrosion behaviour of cold sprayed SS 316L coatings. J Mater Sci 44(9):2320–2326. https://doi.org/10.1007/s10853-008-3200-2
101. Sun Z, Tan X, Tor SB, Yeong WY (2016) Selective laser melting of stainless steel 316L with low porosity and high build rates. Mater Des 104:197–204. https://doi.org/10.1016/j.matdes.2016.05.035
102. Tucho WM, Lysne VH, Austbø H, Sjolyst-Kverneland A, Hansen V (2018) Investigation of effects of process parameters on microstructure and hardness of SLM manufactured SS316L. J Alloys Compd 740:910–925. https://doi.org/10.1016/j.jallcom.2018.01.098
103. Yin S, Jenkins R, Yan X (2018) Microstructure and mechanical anisotropy of additively manufactured cold spray copper deposits. Mater Sci Eng A. https://doi.org/10.1016/j.msea.2018.07.096
104. S. J. Merkt, (2015) Qualifizierung von generativ gefertigten Gitterstrukturen für maßgeschneiderte Bauteilfunktionen. p. 167
105. Yadroitsev I, Krakhmalev P, Yadroitsava I, Johansson S, Smurov I (2013) Energy input effect on morphology and microstructure of selective laser melting single track from metallic powder. J Mater Process Technol 213(4):606–613. https://doi.org/10.1016/j.jmatprotec.2012.11.014
106. Joguet D, Danlos Y, Bolot R, Montavon G, Coddet C (2014) Modeling and measurement of the effective young modulus of porous biomedical materials manufactured via SLM. Local Mech Properties X 606:125–128. https://doi.org/10.4028/www.scientific.net/KEM.606.125
107. Benito JA, Jorba J, Manero JM, Roca A (2005) Change of Young's modulus of cold-deformed pure iron in a tensile test. Metall Mater Trans A 36(12):3317–3324. https://doi.org/10.1007/s11661-005-0006-6
108. Saini M, Singh Y, Arora P, Arora V, Jain K (2015) Implant biomaterials: a comprehensive review. World J Clin cases 3(1):52–57. https://doi.org/10.12998/wjcc.v3.i1.52